Title

Proposed mechanisms for the oxidation of methane into methyl hydrogen sulfate with transition metal species of vanadium or silver

Author

Iniguez, Jesus Alberto

Publication Date

2022

Peer reviewed|Thesis/dissertation

UNIVERSITY OF CALIFORNIA

Los Angeles

Proposed mechanisms for the oxidation of methane into methyl hydrogen sulfate with transition metal species of vanadium or silver

A dissertation submitted in partial satisfaction of the requirements for the degree Doctor of Philosophy in Chemistry

by

Jesus Alberto Iñiguez

2022

ABSTRACT OF THE DISSERTATION

Proposed mechanisms for the oxidation of methane into methyl hydrogen sulfate with transition metal species of vanadium or silver

by

Jesus Alberto Iñiguez

Doctor of Philosophy in Chemistry

University of California, Los Angeles, 2022

Professor Chong Liu, Chair

Methane is a gaseous chemical that can be converted into chemicals of interest useful to industry. However, the grand challenge in methane functionalization is the low reactivity of methane combined with the very high reactivity of its products. The high reactivity of its products leads to overoxidation, which in turn leads to low generation of products of interest since over oxidation leads to the formation of carbon dioxide. The goal of my research projects hereafter is to selectively oxidize methane into the chemical methyl hydrogen sulfate (MHS), which can be hydrolyzed into the commodity chemical of methanol. This is done by combining using transition metals catalysts coupled with electrochemistry in a two-chamber electrochemical system. Moreover, another aspect of my projects has been to propose electrochemical mechanisms for the electrochemical reactions. The first part of my dissertation focuses on using a vanadium molecular catalyst (chapter 2) to selectively oxidize methane electrocatalytically into MHS. Similarly, the second part of this dissertation focuses on the selective oxidation of methane into MHS by using

a molecular silver catalyst (chapter 3). Both research projects of vanadium and silver molecular catalysts both use electrochemistry as the driving force at ambient conditions of room pressure and room temperature, however, the electrolyte used in the chemical reactions is not mild. The electrochemical reaction used 98% concentrated sulfuric acid. While room pressure and temperature is a big focus of the projects, there are studies in the research projects that utilize elevated pressures and temperatures. The use of elevated temperatures and pressures allows us to conduct experiments, which can give us an insight into the electrochemical mechanism that is occurring during the electrolysis reactions. To my knowledge, methane oxidation at room temperature and room pressure had not been seen before with a homogenous catalyst, so the innovation of my project is successfully proving that it is possible to oxidize methane at ambient conditions with a homogenous catalyst while proposing an electrochemical mechanism for the reactions.

The dissertation of Jesus Alberto Iñiguez is approved

Miguel Garcia-Garibay

William Gelbart

Xiangfeng Duan

Chong Liu, Committee Chair

University of California, Los Angeles

2022

Dedicated to my mother Reyna, father Ramon, my sister Dannyela, my brother Fernando. Thank you for your constant words of encouragement and your unconditional love and support.

Table of Contents

List of figures

Chapter 2:

Chapter 3:

Acknowledgements

I would like to express my thanks to everyone who has helped me grow as a scientist to attain my Ph.D. Firstly, thank you to my graduate advisor for his constant mentorship and guidance throughout my graduate program experience. I joined the Chong Liu lab in the Fall of 2017 and throughout the years he has provided me with guidance through scientific discussions that has greatly increased my scientific intuition. The skills I learned in the Chong Liu lab have turned me into a scientist that can conduct research independently. I would like to thank my committee members, Professor William Gelbart, Professor Miguel Garcia-Garibay, and Professor Xiangfeng Duan for their advice and guidance throughout my graduate school experience. I would also like to express my thanks to Dr. Benjamin Papandrea, Dr. Dan Baumann, Dr. Frank Song, and Dr. Dan Zhu who were my graduate student mentors when I was an undergraduate conducting research at UCLA. The mentoring I received from them allowed me to grow as a scientist and to think critically about science as an undergraduate researcher. Lastly, I would like to thank all the group members in the Chong Liu Lab, and the following two colleagues that belong to different research groups at UCLA. Thank you Zachary Gvildys and Mackenzie Anderson for both your friendship and your constant help with scientific discussions throughout the years. You have all made my journey to acquire my Ph.D. an enjoyable experience.

VITA

Education

University California Los Angeles **June 2019**
Master of Science, Chemistry

University of California, Los Angeles
Bachelor of Science, Chemistry **June 2017**

Research experience

Graduate student researcher, *UCLA Chong Liu Lab – Los Angeles, CA* 2017 – 2022

- Discovered two types of transition metal species for methane oxidation that led to two distinct publications and patents
- Performed synthesis of nanoparticles or polymers for electrochemical experiments
- Applied coatings to electrodes for electrochemical methane oxidation reactions
- Analysis of chemical composition of electrochemically generated products
- Designed electrochemical systems for single and two chamber electrochemical reactions
- Performed failure analysis/troubleshooting of technical engineering problems
- Analyzed physical failures of electrodes used in electrochemical systems
- Designed electrochemical systems that improved efficiencies of product generation
- Used a variety of spectroscopy techniques to determine kinetics of a chemical species
- Performed and analyzed NMR data for product concentration determination
- Experimented/optimized parameters in my electrochemical system to maximize efficiencies of methane oxidation
- Utilized TEM/SEM to characterize surfaces of nanoparticles
- Characterized and analyzed electrochemical data

Publications

- Xiang, D.; **Iñiguez, J. A**.; Deng, J.; Guan, X.; Martinez, A.; Liu, C.*, Ag^{II}-mediated Electrocatalytic Ambient CH_4 Functionalization Inspired by HSAB Theory. *Angew. Chem. Int. Ed.* **2021**, *60*, 18152−18161
- Deng, J.; Lin, S.-C.; Fuller, J.; **Iñiguez, J. A.**; Xiang, D.; Yang, D.; Chan, G.; Chen, H. M.*; Alexandrova, A. N.*; Liu, C.*. Ambient methane functionalization initiated by electrochemical oxidation of a vanadium (V)-oxo dimer. *Nature Commun.*, **2020**, *11*, 3686.
- Rodrigues, R.M., Guan, X., **Iñiguez, J.A**. *et al.* Perfluoro carbon nano emulsion promotes the delivery of reducing equivalents for electricity-driven microbial CO_2 reduction. *Nat Catal* 2, 407-414 (**2019**)
- Deng J., **Iñiguez, J.A.,** Liu, C. Electrocatalytic nitrogen reduction at low temperature. *Joule.* 846-856 (**2018**)

Honors and Awards

- UCLA Chemistry Department Michael E. Jung Teaching Award
- UCLA Equity Diversity and Inclusion Award
- Eugene Cota-Robles Fellowship UCLA
- UCLA PhD Competitive Edge Summer Program
- National Institutes of Health (NIH) Maximizing Student Development (MSD) Fellowship
- Jack Kent Cooke STEM Scholar, John Davenport Scholarship

CHAPTER 1: General Introduction

Significance:

Methane is an abundant gaseous chemical, but after oxidizing methane, its highly reactive intermediates hinder its use for practical applications in fuels and commodity chemicals because the intermediates get overoxidized into the final product of Carbon dioxide (CO_2)[1]. Currently the steam reforming and synthesis gas (syngas) method is the industrial method for methanol generation from methane[2,3,6] . The steam reforming process is an endothermic reaction that uses methane and water to generate carbon monoxide and hydrogen gas intermediates known as syngas[3,6]. Following the generation of syngas, the hydrogen and carbon monoxide gases are used with a copper and zinc oxide catalyst supported on an alumina that will generate methanol[3,6]. This process requires high temperatures and high pressures along with a financially expensive infrastructure[1-3]. To my knowledge, presently there is no industrial process for the conversion of methane to methanol that is cost-effective[4]. Therefore, finding alternative and cost-effective methods for the oxidation of methane to methanol is of high interest to many researchers. Electrochemistry serves as an attractive alternative approach because it can be powered by renewable energy sources as well as being a relatively inexpensive method when compared to the expensive steam reforming and syngas method. To my knowledge there are no reports of methane oxidation at room temperature with a homogenous transition metal catalyst: the innovation of my projects is the production of methyl hydrogen sulfate (MHS) at room temperature and ambient pressure with a vanadium molecular catalyst (Chapter 2) and a molecular Silver (Ag) catalyst (chapter 3).

Electrochemical Methane oxidation:

The grand challenge in methane oxidation is the poor conversion of methane and poor selectivity of products. Many efforts have been made to achieve higher conversion rates of methane into methanol along with higher selectivity as well. Previously in the past it has been reported that transition metal catalysts can activate (i.e. break) the Carbon-Hydrogen (C—H) bond[1,2,4,5] making them attractive homogenous catalysts for selective product generation. Moreover, it has been hypothesized previously by other research groups that high valent electrophilic metal ion intermediates are influential in the activation of C—H bonds[1,4,5]; expanding on this hypothesis, it is further hypothesized that by varying the electrode potential in an electrochemical system then a nonequilibrium population of highly reactive ions can possibly be generated for methane functionalization[1,4,5]. After experimenting with a couple different transition metal catalysts in the laboratory, we found that vanadium works as one of these catalysts to selectively oxidize methane. On a different project we have also seen that silver also works to selectively oxidize methane into MHS, which can be seen in the following chapters 2 and 3. MHS is a chemical of interest in these projects because MHS can be hydrolyzed into methanol[5].

References

1. O'Reilly M.E.; Kim R.S.; Oh S.; Surendranath Y. Catalytic Methane Monofunctionalization by an Electrogenerated High -Valent Pd Intermediate. ACS Cent. Sci. 2017, 3, 1174 −1179.

2. Periana R.A.; Taube D.J.; Gamble S.; Taube H.; Satoh T.; Fujii H. Platinum catalysts for the high - yield oxidation of methane to a methanol derivative. Science. 1998, 280, 560 -564

3. Lunsford J.H. Catalytic conversion of methane to more useful chemicals and fuels: a challenge for the 21st century. Catalysis Today . 2000, 63, 165 – 174

4. Latimer A.A.; Kakekhani A.; Kulkarni A.R.; Nørskov J.K.; Direct Methane to Methanol: The Selectivity−Conversion Limit and Design Strategies. ACS Catal. 2018, 8, 6894 −6907.

5. Gunsalus N.J.; Koppaka A.; Park S.H.; Bischof S.M.; Hashiguchi B.G.; Periana R.A. Homogenous Functionalization of Methane. Chem. Rev. 2017, 117, 8521 −8573.\

6. Ma M.;Jin B.J.; Li P.;Jung M. S.;,Kim J, I.; Cho Y.; Kim S.; Moon J.H.;, Park J.H.; Ultrahigh Electrocatalytic Conversion of Methane at Room Temperature. Adv. Sci. 2017, 4, 1700379

7. Rahim M. H. A.; Forde M.M.; Jenkins R.L.; Hammond C.; He Q.; Dimitratos N.; Lopez - Sanchez J.A.; Carley A. F.; Taylor S.H.; Willock D. J.; Murphy D.M.; Kiely C.J.; Hutchings G.J. Oxidation of methane to methanol with hydrogen peroxide using supported gold -palladium alloy nanoparticles. Angew. Chem. Int. Ed . 2013,52, 1280 –128

CHAPTER 2: Electrocatalytic oxidation of methane to methyl hydrogen sulfate with vanadium oxo-dimer

This chapter is a version of: Deng, J., Lin, SC., Fuller, J., Iñiguez, J,A. *et al.* Ambient methane functionalization initiated by electrochemical oxidation of a vanadium (V)-oxo dimer. *Nat Commun* **11,** 3686 (2020).

2.1 Introduction

Natural gas resources have a lot of undesirable loss of methane (CH_4) gas especially at remote locations by emissions into the atmosphere or by the burning of methane gas (i.e. flaring)[1,2]. These have been common practices over decades that are wasteful since methane gas can possibly be converted into commodity chemicals as aforementioned. One possible strategy to minimize this wastefulness is to attempt to convert CH_4 into liquid chemicals at the source of emission under ambient conditions such as room pressure and room pressure[2]. For this to be possible the following requirements must be met. Firstly, a kinetic requirement of a low activation energy barrier. Secondly, a high reactivity that will allow the chemical reaction to move forward under a low thermal energy and partial pressure of CH_4 at mild conditions such as room pressure and room temperature. In the past and currently CH_4 functionalization occurs at high pressure and elevated temperatures. Additionally, the functionalization of CH_4 [3-16] can involve metal-catalyzed reactions [3-7], superacid-based activation [17], or a free radical chain mechanism catalysis performed by a peroxo species [8-10]. For previous work in this field, a metal catalyzed reactions reported by Periana and coworkers shown in Fig. 1a [3-6] demonstrates an electrophilic activation of CH_4 using a palladium (Pd) or platinum (Pt) metal species at elevated pressures and elevated temperatures. The electrophilic activation is followed by an oxidation process that regenerates the active sites on the catalytic metal species. However, at ambient

conditions such as room temperatures and room pressures, the metal species are not able to activate CH_4. However, in the approaches based on radical chain mechanism shown in Fig. 1b [8-10], initiators including peroxo species yield oxygen radicals that are able activate CH_4 at room temperature with low activation energies [18]. Notwithstanding of these results, it is not easy to achieve a stable selective catalytic process that generates and replenishes the radical species. The balancing the reactivity and regeneration of active species is a grand challenge that requires alternative approaches for ambient CH_4 functionalization.

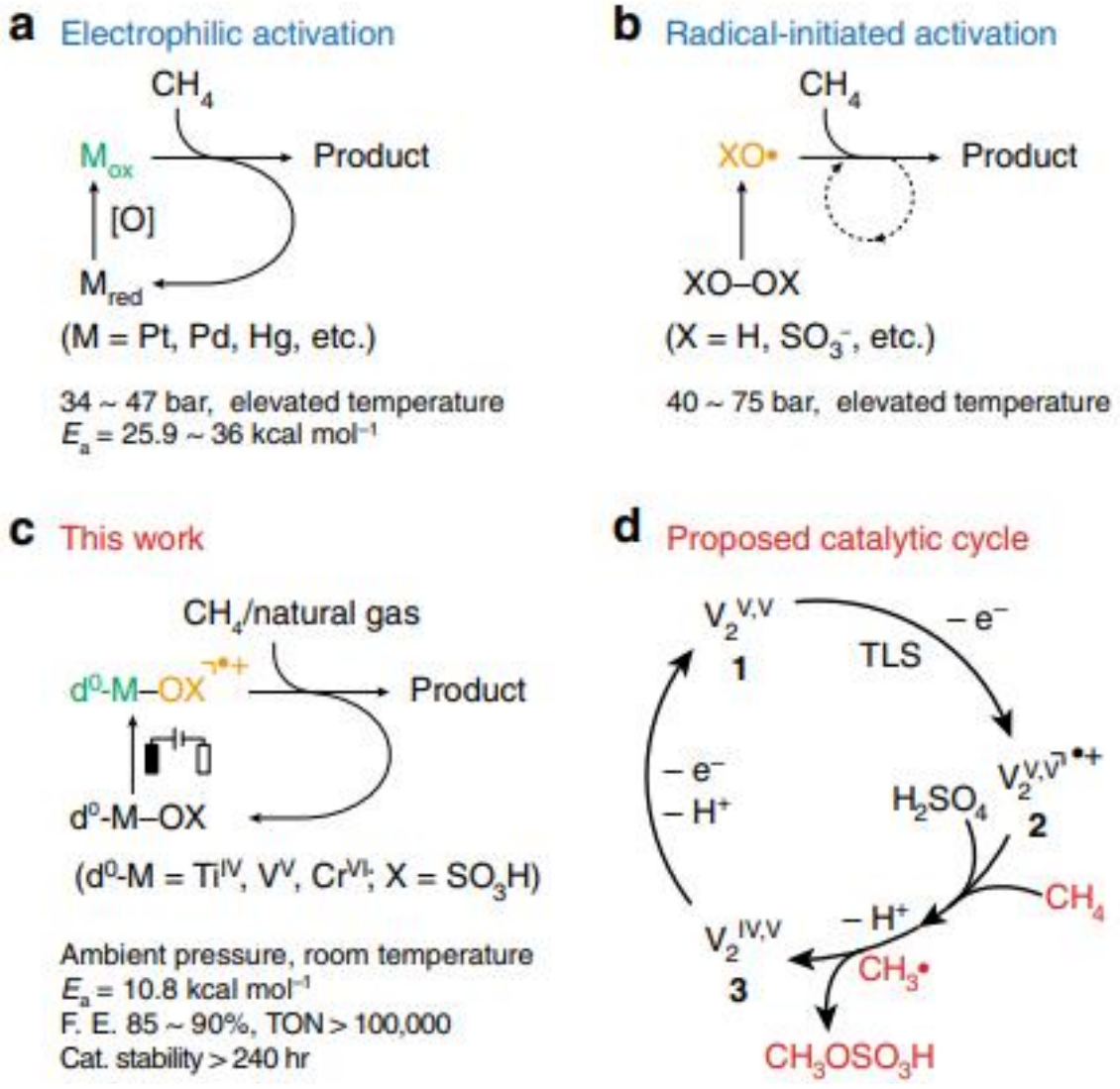

Figure 2.1: (**a–c)** Representative approaches of CH_4 functionalization based on electrophilic activation[3,4,5,6] (**a**) and radical chain mechanism[8,9,10] (**b**), in comparison with the proposed electrocatalytic method **(c)**. **(d)** The proposed catalytic cycle of electrocatalytic CH_4 activation with d^0 vanadium (V)-oxo dimer (**1**). M_{red} and M_{ox}, reduced and oxidized metal active sites, respectively; [O], chemical or electrochemical oxidation; E_a, activation energy; d^0–M, d^0 early transition metal species; F.E. Faradaic efficiency, TON turnover number, TLS turnover-limiting step

Here we propose that a controlled electrochemical generation of oxygen radicals that addresses the challenge mentioned previously. The electrochemical reduction-oxidation (redox) process provides a way of generating and replenishing radical species at ambient conditions without sacrificing high reactivities [19,20]. To my knowledge, d^0 early transition metal centers are not known to be directly oxidized, this oxidation reaction was a serendipitous discovery. What we found was that electrochemical oxidation of d^0 early transition metal-oxo species in 68–98% H_2SO_4 generate cation radicals on the sulfonic ligand that selectively oxidizes CH_4 at room pressure and room temperature (Fig. 1c). Here we report that d^0 vanadium (V)-oxo dimer ($V_2^{V,V}$, **1**) [21] as the model catalyst for mechanistic understanding as seen in Fig. 1d.

2.2 Experimental

Chemicals and materials: All chemicals were purchased from Sigma-Aldrich, Thermo Fisher Chemical, or VWR International, unless otherwise stated. All chemicals were used as received unless specified. Dimethyl sulfoxide-d_6 (DMSO-d_6) was purchased from Cambridge Isotope Laboratories, Inc. All deionized (DI) water was obtained from a Millipore Milli-Q Water Purification System. Fluorine-doped Tin Oxide (FTO) glass was purchased from Hartford Glass Incorporation. CH_4 (99.5%) was purchased from Airgas, C_2H_6 (99%), C_3H_8 (98%), and $^{13}CH_4$

(99%; 99 atom% ^{13}C) were purchased from the Sigma-Aldrich. Natural gas mixture was obtained from the outlet in Molecular Science Building 4211, Department of Chemistry and Biochemistry, UCLA, which is supplied via pipeline by SoCalGas. SRI multiple gas analyzer #5 gas chromatograph (GC), 8610C is used to analyze the natural gas mixture. The components are 91.78 mole% CH_4, 4.31 mole% C_2H_6, 0.31 mole% C_3H_8, 0.04 mole% n-C_4H_{10}, 0.03 mole% i-C_4H_{10}, 0.01 mole% n-C_5H_{12}, 0.01 mole% i-C_5H_{12}, and 0.81 mole% CO_2. Unless specifically noted, reagent-grade 98% H_2SO_4 (VWR BDH3074-3.8LP) was employed as the solvent, which contains 5 ppm of metal impurities. When needed, we also employ high-purity 98% H_2SO_4 (Sigma-Aldrich 339741), which contains 0.3 ppm of metal impurities as shown in the product certificate.

Catalyst preparation: Homogeneous bimetallic catalyst **1** was prepared by dissolving vanadium pentoxide (V_2O_5) in 98% H_2SO_4 with ultra-sound treatment for 6 h. Homogeneous titanium (IV)-oxo and chromium (VI)-oxo catalysts were prepared by dissolved titanyl sulfate ($TiOSO_4$) and potassium chromate (K_2CrO_4) in 98% H_2SO_4, respectively. The heterogeneous variant **4** ($VOPO_4{\cdot}2H_2O$) was prepared based on previous literature [37,40]. V_2O_5 (4.8 g), H_3PO_4 (85.5%, 26.6 mL), and H_2O (115.4 mL) were refluxed at 110 °C for 16 h. After gently cooling down to room temperature, the yellow precipitate in the mixture was collected by filtration and washed several times with water and acetone. The resulting sample was dried in an oven at 100 °C for 3 h. When **4** was investigated for its electrochemical response, **4** was loaded onto a FTO electrode via a dip-coating procedure. A dispersion of **4** was prepared at a concentration of 6 mg mL^{-1} in 2-propanol. The yellow dispersion was ultrasonicated for 30 min until the color of the dispersion became faded. Afterwards, sodium carboxymethyl cellulose (CMC) was added into the dispersion (weight ratio of $VOPO_4{\cdot}2H_2O$: CMC = 80: 5). The mixture was stirred at 600

revolution per minute (rpm) on the heating plate to remove excess 2- propanol and form a homogenous slurry, which was then dip-coated onto FTO at a loading amount of 1.9 mg cm^{-2} for **4**

Chemical and material characterizations: Ultraviolet–visible (UV–vis) spectra was conducted on Hewlett-Packard 8453 UV–vis spectrophotometer. Proton NMR (^{1}H-NMR) and carbon NMR (^{13}C-NMR) were recorded on a Bruker AV400 (400 MHz) spectrometer. Deuterium NMR (^{2}D-NMR) was recorded on a Bruker AV500 (500 MHz) spectrometer. Vanadium NMR (^{51}V-NMR) was performed on an Agilent DD2 600 (600 MHz) spectrometer. Powder X-ray diffraction (XRD) patterns were measured on a Panalytical X'Pert Pro X-ray Powder Diffractometer with a Cu Kα source (λ = 1.54178 Å), The intensities were recorded within the 2θ range from 10° to 60° with a voltage of 45 kV, and a current of 40 mA. Scanning electron microscope image was measured with a JEOL JSM 6700F instrument. XANES and EXAFS were recorded at BL17C of National Synchrotron Radiation Research Center (NSRRC), Hsinchu, Taiwan. Gas chromatography–mass spectrometry (GC-MS) was performed on Agilent 6890-5975 GC-MS with Inert XL Selective Detector. The GC is equipped with a capillary HP-5MS column (Model No.: 19091S-433, 30.0 m × 250 μm × 0.25 μm). The instrument is operated with an oven temperature of 50 °C, an inlet temperature of 280 °C, and a flow rate of 1.2 mL min^{-1} with helium carrier gas. A split/splitless injector is applied with a split ratio of 5:1 and a split flow of 5 mL min^{-1}. The MS has a source temperature of 230 °C and a quadrupole temperature of 150 °C. The SRI multiple gas analyzer #5 GC is equipped with 3 S.S. columns including 18″ Hayesep D, 3′MS 5A and 6′ Hayesep D. The instrument is operated with an oven temperature of 50 °C, a temperature profile from 50 to 270 °C, and a flow rate of 40 mL min^{-1} at 15 psi with argon

carrier gas. X-ray photoelectron spectroscopy (XPS) was measured on a Kratos AXIS Ultra spectrometer (Kratos Analytical, Manchester, UK)**.**

Electrochemical characterization: All electrochemical experiments were recorded using a Gamry Instruments Reference 600+ and Interface 1000 potentiostats. Unless mentioned specifically, a three-electrode setup was applied with a Pt wire pseudo-reference electrode and a Pt counter electrode. The Pt pseudo-reference electrode was calibrated to a Hg_2SO_4/Hg (saturated K_2SO_4) reference electrode (CH Instrument, Inc.) via the measurement of open-circuit potentials. The relationship is E (V vs. Hg_2SO_4/Hg) = E (V vs. Pt) + 0.755 V. The gas environment of the electrochemical cell was controlled either CH_4 (Airgas, 99.5%) or N_2 (Airgas, 99.999%), which were bubbled into the reactor at rates of 7.2 (CH_4) and 10 (N_2) standard cubic centimeters per minute (sccm) with the use of a mass flow controllers (Omega Engineering, Inc., FMA5510A). The data were reported after iR compensation. Unless noted specifically, the electrolyte is 98% H_2SO_4 with a certain vanadium concentration of **1**.

Quantification of liquid products: ^{1}H-NMR was applied to quantify product accumulation in DMSO-d_6 using acetic acid (CH_3COOH) as the internal standard. Total, 0.4 mL liquid aliquots from electrolysis were mixed with 0.1 mL DMSO-d_6 prior to the measurements. Chemical shifts are reported on a parts-per-million (ppm) scale. Methyl bisulfate (CH_3OSO_3H) exhibits a singlet at 3.34 ppm while the singlet from acetic acid (CH_3COOH) peak resides at 1.96 ppm. A calibration curve was constructed by determining the relative ratio of integrated area between the NMR peaks of CH_3OSO_3H and CH_3COOH. Product quantification of C_2H_6, C_3H_8, and natural gas mixture follows the same protocol, except for the quantification of CH_3COOH as a C_2 product from C_2H_6. The quantification of CH_3COOH as a C_2 product was fulfilled by adding a known concentration of CH_3OSO_3H as an internal standard in a separate ^{1}H-NMR measurement.

Calculation of Faradaic Efficiency (F.E.): The F.E. of bulk electrolysis was calculated based on the following equation

$$\text{F.E.} = \frac{nFC_{Product}V_{Solution}}{overall\ charge} x100\%$$

Here, F is the Faraday's constant, $C_{Product}$ is the concentration of product after bulk electrolysis, $V_{Solution}$ is the total electrolyte volume, and the overall charge is the total electric charges passed through the working electrode. The variable n in the equation is the number of electrons required in order to generate one product molecule by electrochemistry. n = 2 for the formation of methyl hydrogen sulfate (CH_3OSO_3H) from CH_4. n = 2 and 6 for the formation of ethyl hydrogen sulfate ($C_2H_5OSO_3H$) and acetic acid (CH_3COOH) from C_2H_6, respectively. n = 2 and 4 for the formation of isopropyl hydrogen sulfate (i-$C_3H_7OSO_3H$) and acetone (CH_3COCH_3) from C_3H_8, respectively.

Calculation of TOF and TON: In the following we provide the protocols that we calculate the turnover frequencies (TOF) and turnover numbers (TON) for the reported data, based on the methods established in prior literature[19,23]. The diffusion coefficient for 1 (D) was determined from the cyclic voltammgrams based on the Randles–Sevcik equation shown below

$$j_p = 0.4463nFC_{Cat}(\frac{nFvD}{RT})^{\frac{1}{2}}$$

Here j_p is the peak current density of quasi-reversible redox couple, n is the number of electrons transferred in the redox event, F is the Faraday's constant, C_{Cat} is **1**'s concentration, v is the scan rate, R is the gas constant, and T is the temperature of experiment. As derived from Supplementary Fig. 1a, b, D = 2.18×10^{-7} cm^2 s^{-1} for species **1** in the electrolyte.

The observed TOF of bulk electrolysis was determined based on the following equation shown below [19,23]

$$TOF = (\frac{j_{Product}}{nFC_{Cat}})^2 \frac{1}{D}$$

Here, $j_{Product}$ is the partial current density of product formation in bulk electrolysis, n is the number of electrons required to generate one product molecule, F is the Faraday's constant, C_{Cat} is the concentration of catalyst **1**, D is the diffusion coefficent of catalyst (2.18×10^{-7} cm^2 s^{-1} for species **1** as determined above.

The TON of bulk electrolysis was determined based on the following equation[19,23]:

$$TON = \frac{C_{Product}V_{Solution}}{AC_{Cat}} \sqrt{\frac{TOF}{D}}$$

Here, $C_{Product}$ is the product concentration after bulk electrolysis, $V_{Solution}$ is the total electrolyte volume, A is the electrode area, C_{Cat} is the concentration of catalyst **1**, D is the diffusion coefficent of catalyst (2.18×10^{-7} cm^2 s^{-1} for species **1** as determined above), and TOF is the TOF calculated based on above protocol. On the condition of a homogenous process with molecular catalyst **1**, the diffusion coefficient extracted from the V(V)/V(IV) redox couple is a reasonable approximate of the real catalytic redox couple, the vanadium(V)-oxo dimer and its one-electron-deficient cation radical, because we are unable to characterize the cation radical due to its transient nature. Here, we offer a rough estimate of the relative uncertainty of such an approximation based on our proposed mechanism. The Stokes–Einstein relationship[41] predicts that the diffusion coefficient D of similar molecules follows: $D \sim MW^{-1/3}$, in which MW is the molecular weight. As MW = 538.16 g mol^{-1} for **1**, the relative uncertainty of D in our procedure

is about 6% or 12%, assuming the loss of one or even two of the sulfonic ligands, respectively. As the TOF ~D^{-1} [23], at most about 10% relatively uncertainly will incur in our practice.

Computational method: All calculations were performed with Turbomole[42-52] using the M06 density functional[53]. The def2-SVP basis set was used for geometry optimizations and free energy corrections, and the def2-TZVP basis set was used for electronic energies[54]. Solvation was modeled with COSMO[55] with the dielectric constant set to 101[56]. Images were rendered using Chemcraft[57]. The natural bond orbital (NBO) analysis was used for atomic charge calculations[36].

Details of XAS experiments: XAS, including X-ray absorption near edge spectra (XANES) and extended X-ray absorption fine structure (EXAFS), at V K-edge were collected in total-fluorescence-yield mode at ambient conditions at BL17C of National Synchrotron Radiation Center (NSRRC), Hsinchu, Taiwan. Spectra were recorded in the energy range from −100 to 600 eV, relative to that of V K-edge absorption (5465.0 eV). The XAS spectra were processed by subtracting the baseline of pre-edge and normalizing that of post-edge. EXAFS analysis was carried out using Fourier transform on k^3-weighted EXAFS oscillations to assess the contribution of each bond pair to Fourier transform peak. The curve fitting of EXAFS spectra was conducted using the software, REX2000, with FEFF program. The operando XAS experiments at V K-edge were conducted under the same procedure at TPS beamline 44A of NSRRC, Hsinchu, Taiwan. A three-electrode arrangement was used during the operando measurements. The electrolyte was saturated with 1-bar CH_4, and the measurements were performed using an Autolab PGSTAT204 potentiostat (Metrohm Autolab) in a customized reactor.

Operando Raman characterization: A three-electrode setup in a home-made cell was adopted for Operando Raman spectroscopy and the electrochemical measurements. The measurements in

a CH_4-saturated electrolyte were recorded using a Raman microscopy (UniNano UNIDRON) and an Autolab PGSTAT204 potentiostat (Metrohm Autolab). A laser of 633 nm with a spot size of ~1 μm^2 served as the excitation source, and the output power was 2.5 mW. A 50x objective lens was employed for operando measurements during electrolysis, while all results were obtained under an exposure duration of 3 s with the accumulation number of 60 times.

2.3 Results and Discussion:

As previously mentioned, the d^0 vanadium (V)-oxo catalyst (**1**) was prepared by dissolving V_2O_5 in 98% H_2SO_4. As displayed in figure 2a cyclic voltammograms of 10 mM **1** in 98% H_2SO_4

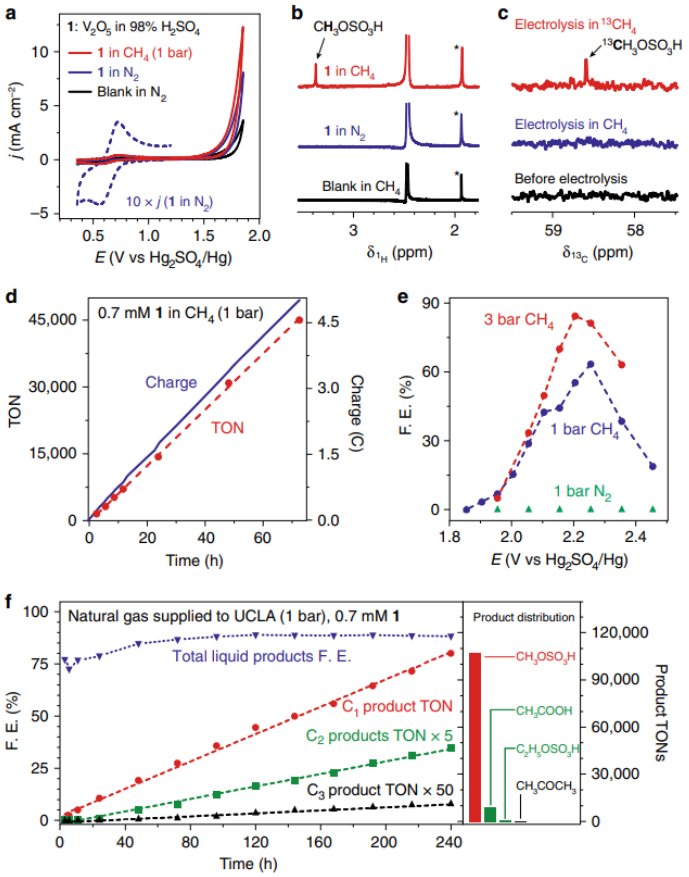

Figure 2.2: **a**, **b** Cyclic voltammograms **(a)** and ^{1}H-NMR spectra of liquid samples after 6 h electrolysis **(b)** for 10 mM **1** in 1 bar CH_4 (red), 10 mM **1** in 1-bar N_2 (blue), and blanks

without **1** (black). Dashed blue, current density (*j*) of blue trace magnified by a factor of 10. *, internal standard acetic acid. **(c)** ^{13}C NMR spectra of samples before (black) and after electrolysis with $^{13}CH_4$ (red) and CH_4 of natural abundance (blue), respectively. **(d)** Calculated TONs (red) and electric charges passed (blue) versus the duration of electrolysis. **(e)** F.E. of CH_4 functionalization in 10 mM **1** vs. electrode potential *E* under 1 bar N_2 (green), 1 bar CH_4 (blue) and 3-bar CH_4 (red). **(f)** Cumulative TONs for C_1 (red), C_2 (green, multiplied by a factor of 5), and C_3 products (black, multiplied by a factor of 50) as well as F.E. values of total liquid products (blue) are plotted against the duration of bulk electrolysis. TON values for CH_3OSO_3H (red), CH_3COOH plus $C_2H_5OSO_3H$ (green), and CH_3COCH_3 (black) within 240 h are shown on the right, respectively. Natural gas mixture supplied by SoCalGas was used as the substrate at ambient pressure. Trace products beyond C_3 were also observed. 100 mV s^{-1} and Pt working electrode in (a); FTO working electrode in (b) to (f), and $E = 2.255$ V vs. Hg_2SO_4/Hg in (b) to (d), and (f).

under 1 bar nitrogen gas (N_2) (blue), 1 bar CH_4 (red), and a blank control (black) are displayed, the experiments are conducted at a temperature of 25 °C on a platinum (Pt) working electrode. A quasi-reversible peak corresponding to V^{V}/V^{IV} redox couple was observed with a midpoint potential of $E_{1/2}$ = 0.644 V vs. Hg_2SO_4/Hg reference electrode, with a diffusion coefficient D = 2.18×10^{-11} m^2 s^{-1} for **1** based on Randles–Sevcik analysis, which can be found on the supplementary information of this publication as Fig. 1a, b.. Moreover, additional oxidation current of **1** was observed at an electrochemical potential E > 1.6 V vs. Hg_2SO_4/Hg, and it was observed that an oxidation current is greater in the presence CH_4 relative to that when N_2 gas is present in the electrochemical system. This suggests that **1** can be further oxidized

electrochemically, and the reactive species generated can likely react with CH_4. Bulk electrolysis in 98% H_2SO_4 under 1 bar CH_4 was conducted at a potential E = 2.255 V vs. Hg_2SO_4/Hg for 6 h with a working electrode of fluorine-doped tin oxide (FTO). Analysis of the liquid composition after electrolysis was analyzed by nuclear magnetic resonance (NMR) spectroscopy, specifically ^{1}H-NMR and ^{13}C-NMR. CH_3OSO_3H, which can yield methanol after hydrolysis, was observed at a chemical shift of δ = 3.34 ppm in ^{1}H-NMR after electrolysis with 10 mM **1** under CH_4 (red color in Fig. 2b). Furthermore, no gaseous or liquid products besides CH_3OSO_3H was observed as a product of CH_4 oxidation within our detection limit when conducting NMR spectroscopy (Fig. 2b). Other spectroscopies such as mass spectroscopy and gas chromatography were utilized to further prove this; the information can be found in the supplementary information of this publication as supplementary Fig. 2a, b and supplementary Fig. 3, respectively. It is important to note that organic products of interest were not detected when **1** was not present in the electrochemical system under CH_4 (black), with 10 mM **1** under N_2 (blue in Fig. 2b), or at an anodic potential less than (E = 1.855 V vs. Hg_2SO_4/Hg) (Supplementary Fig. 2d). The previous results confirm that CH_4 undergoes a two-electron oxidation into CH_3OSO_3H, which is initiated by the electrochemical oxidation of **1**. Additionally, the absence of a well-defined redox wave preceding the current onset in Fig. 2a suggests two potential scenarios of a homogenous electrocatalysis limited by the rate of electron transfer or the occurrence of materials deposition during the scans of cyclic voltammetry. These results suggest a likely homogenous electrocatalysis limited by charge transfer. We also conducted isotope-labeling experiments by introducing $^{13}CH_4$ as the substrate at a pressure of 1 bar. It was observed that the presence of $^{13}CH_4$ versus CH_4 of natural abundance leads to the surge of $^{13}CH_3OSO_3H$ signal at δ = 58.6 ppm in ^{13}C-NMR after electrolysis (Fig. 2c).

Another aspect of the project was to study the electrochemical CH_4 and natural gas functionalization when an electrochemical potential is applied. The electrocatalysis with **1** demonstrated that it selectively functionalized CH_4 and has high turnover numbers (TONs) and turnover frequencies (TOFs). Bulk electrolysis was conducted with a concentration of 0.7 mM **1** at 25 °C under 1 bar pressure of CH_4. Liquid aliquots at different time points were analyzed, and the electrochemical TONs were calculated based on the existing method[19,23]. Figure 2d shows the amount of electric charge and the calculated TON's as a function of time of the electrolysis. A linear correlation suggests a durable catalyst of TON up to 45,000 without a sign of catalyst degradation in the observed time of 72 h. We also investigated the Faradaic efficiency (F.E.), which is defined as the selectivity of converting CH_4 into CH_3OSO_3H based on the amount of electric charge as function of E at 25 °C. In 10 mM **1** (Fig. 2e), the absence of CH_4 leads to no product formation (green), and under 1 bar CH_4 an optimal F.E. of 63.5% is seen with a potential of E = 2.255 V vs. Hg_2SO_4/Hg (blue). It was observed that the reaction selectivity has a mass transport limitation and a limited solubility of CH_4 in solvent (~1 mM)[11]. Moving forward to in the project, different pressures of the electrochemical system were studied. When CH_4 pressure increased to 3 bar, we observed an F.E. = 84.5% at E = 2.205 V vs. Hg_2SO_4/Hg (red in Fig. 2e). The corresponding TOFs of **1** as an electrocatalyst are 483 and 1336 h^{-1} for CH_4 at pressures of 1 bar and 3 bar, respectively, which are conservative and underestimated given the nature of our analysis as stated in the Supplementary Note 1 found in the supplementary information of this publication. Furthermore, the measured TOF values at room temperature compare well relative with other reported catalysts at elevated temperatures and high pressures, this can be seen in Supplementary Table 1 of the supporting information of this publication. Additionally, natural gas studies were conducted with **1** to compare how **1** effect gaseous species such as ethane

(C_2H_6) and propane (C_3H_8), which can be found in natural gas. The results of this can be further seen in the journal publication.

The reported catalyst **1** can yield a high product concentration capable for practical implementations. The limited solubility of CH_4 in the solvent within current batch reactor[11], electrocatalytic experiments of higher product concentrations were conducted under room temperature at 11 bar CH_4 pressure to to minimize the mass transport issue of limited gas solubility. A 72 h electrolysis reaction leads to a CH_3OSO_3H concentration of ~110 mM with F.E. = 81.2% (E = 2.376 V vs. Hg2SO4/Hg). Adding 1 M CH_3OSO_3H prior to the electrocatalysis under the same condition does not hinder the catalysis or decompose the pre-added CH_3OSO_3H. A single-pass conversion of 1% was observed in the mixed-flow electrochemical reactor, comparable to the results that lead to electrochemical reduction of CO_2 and CO at near-industrial level[27,28]. The product concentrations reported here are higher than the ones in other electrocatalysis[5,6], and suggest that high product concentration of electrocatalysis is attenable. There seems no observable fundamental limit for product concentrations exceeding one mole per liter, a threshold considered suitable for industrial applications[11].

The attractive features of catalyst **1** led us to investigate the underlying mechanism during electrolysis with CH_4 as the substrate. The current density corresponding CH_3OSO_3H formation (j_{CH4}), a surrogate of CH_4-activating rate, was investigated as a function of catalyst concentration **[1]** (Fig. 3a), the electrode potential E (Fig. 3b), the partial pressure of CH_4 (p_{CH4}) (Fig. 3c), and the temperature T (Fig. 3d). A linear relationship with a slope = 1.03 ± 0.08 between $\log_{10}(j_{CH4})$ and $\log_{10}$(**[1]**) suggests that CH_4 activation is first-order on **1** (Fig. 3a). When $\log_{10}(j_{CH4})$ was plotted against E (Fig. 3b), a Tafel slope of about 120 mV dec^{-1} was observed before j_{CH4} plateaus at larger E values as CH_4 is depleted near electrode. This suggests that the first electron

removal from **1** is the TLS, uncommon for homogeneous electrocatalysis (Supplementary Note 2). The overlapping points under 1 bar and 3 bar CH_4 pressure when E < 2.1 V vs. Hg_2SO_4/Hg suggest that CH_4 is not involved in the TLS or any pre-equilibrium steps. When E > 2.1 V vs. Hg_2SO_4/Hg, a linear relationship between $\log_{10}(j_{CH4})$ and $\log_{10}(p_{CH4})$ with a slope of 0.91 ± 0.07

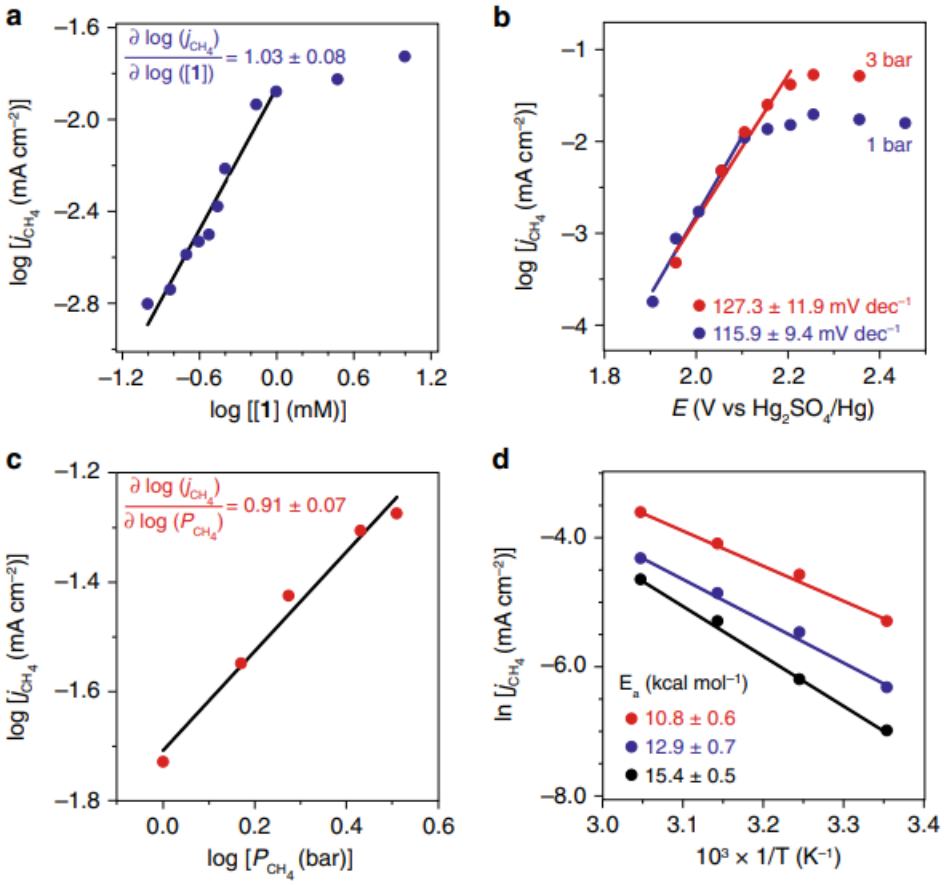

Figure 2.3: (a) The logarithmic of partial current density for CH_4 functionalization, $\log(j_{CH4})$, versus the logarithmic of **1**'s concentration, log ([**1**]). **(b)** $\text{Log}(j_{CH4})$ vs. *E* under CH_4 pressures of 1 bar (blue) and 3 bar (red) with the fitted Tafel slopes displayed. **(c)** $\text{Log}(j_{CH4})$ vs. the logarithmic of CH_4 pressure, $\log(p_{CH4})$. **(d)** The natural logarithmic of partial current density for CH_4 functionalization, $\ln(j_{CH4})$, vs. inverse of temperature, T^{-1}, at 1.955 V (black), 2.005 V (blue), and 2.055 V (red) vs. Hg_2SO_4/Hg, respectively. The corresponding apparent activation

energies (E_a) are displayed. Unless noted specifically, 25 °C, 10 mM **1** in 98% H_2SO_4, E = 2.255 V vs. Hg_2SO_4/Hg, p_{CH4} = 1 bar, data recorded from 6 h bulk electrolysis.

(Fig. 3c) suggests that CH_4 is activated in a first order after the TLS. We also found that the residual current density, the difference between total current density (j_{total}) and j_{CH4}, is independent of p_{CH4} (Supplementary Fig. 2c). It further corroborates that no gaseous or liquid products other than CH_3OSO_3H were generated from CH_4 oxidation, and solvent oxidation into O_2 and possibly trace persulfate[29,30] is the only plausible side reaction. The Arrhenius plot between $\ln(j_{CH4})$ and 1/T yields an apparent activation energy (E_a) as low as 10.8 ± 0.6 kcal mol^{-1} (Fig. 3d), consistent with the observed ambient reactivity. When conducting electrolysis of **1** in 98% D_2SO_4 with CH_4 of natural isotope abundance, 2D and ^{1}H-NMR spectra showed no H/D exchange in the methyl group of product CH_3OSO_3H (Supplementary Fig. 6e). This excludes the possible mechanism induced by an electrochemically generated superacid[17], which should yield significant H/D exchange in the methyl group[11]. In addition, when CH_4 was exposed to **1** in 98% H_2SO_4 with added $K_2S_2O_8$ or H_2O_2 in the absence of electricity, CH_4 functionalization was not observed at ambient conditions (Supplementary Fig. 6f). This illustrates that it is difficult for chemical method to sustainably generate reactive radical intermediates at room temperature, which necessitates our use of electrochemistry as proposed before. It also shows that the possible formation of peroxo species including peroxoacids is not contributing to the observed reactivity. When the electrolyte was switched from 98% H_2SO_4 to oleum with 20% SO_3, a 5.4:1 molar ratio between CH_3SO_3H and CH_3OSO_3H was observed after electrocatalysis (Supplementary Fig. 8). This indicates the formation of CH_3• radical during the catalysis, which yields CH_3SO_3H in the presence of SO_3 [9]. Overall, our experimental data support an electrochemical catalysis of low activation energy. After a turnover limiting one-

electron oxidation of **1**, the oxidized species undergoes a first-order C–H activation in CH_4 and a formation of CH_3• radical (Fig. 1d).

Despite its ease of preparation, the structural information of **1** is not well understood. It was hypothesized to be a $V_2^{V,V}$ dimer with two terminal $V^V{\equiv}O$ moieties connected by a bridging

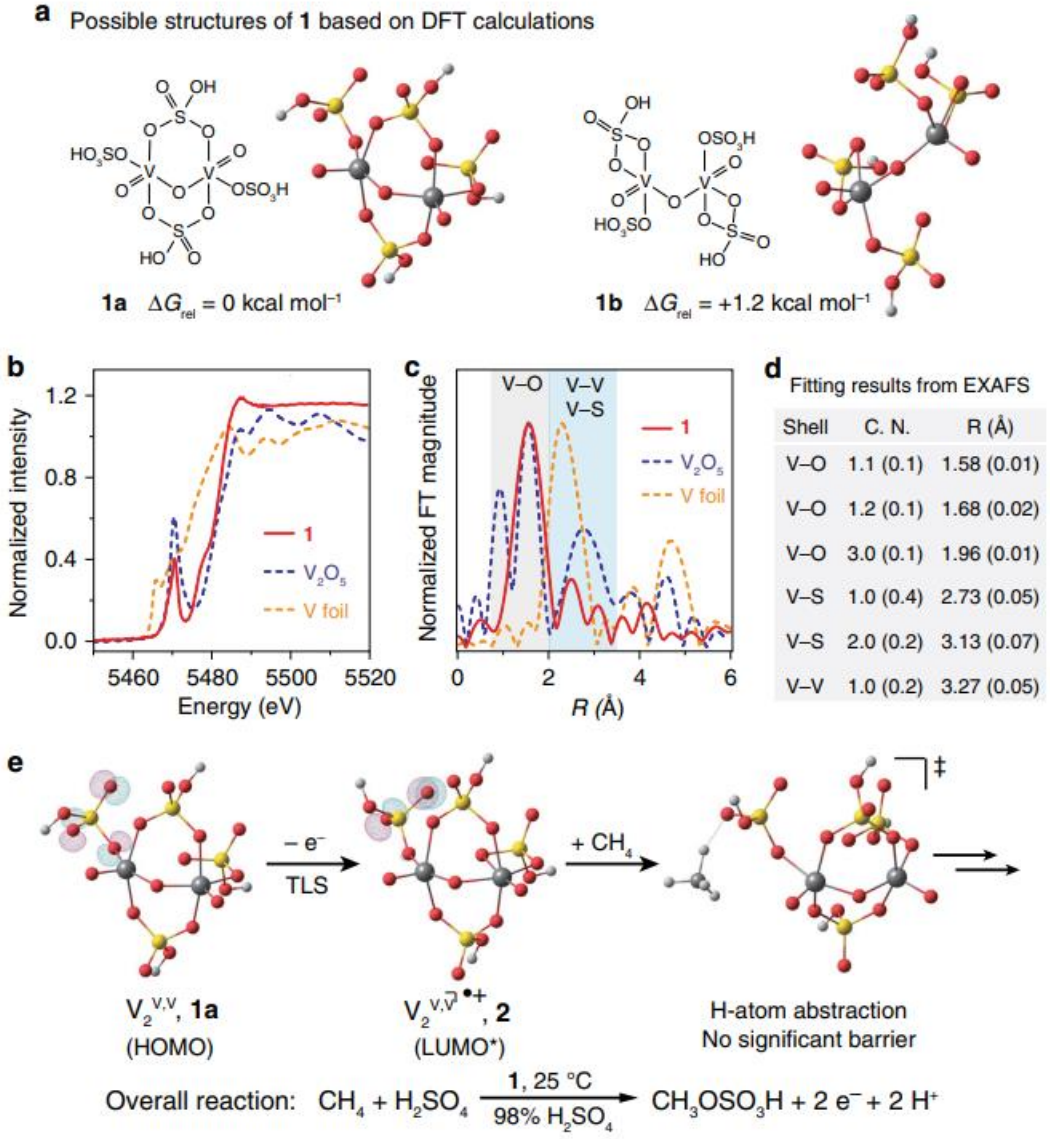

Figure 2.4: Structural information of the catalyst and a proposed mechanism. **(a)** Possible isomeric structures of **1** and their relative energetics based on DFT calculations. **(b, c)**

Normalized intensity of V K-edge X-ray absorption near-edge structure (XANES) **(b)** and extended X-ray absorption fine structure (EXAFS) **(c)** for **1** (solid red), V_2O_5 (dashed blue), and metallic V (dashed yellow). **(d)** Calculated coordination number (C.N.) and the distance (R) away from V atom based on EXAFS results. **(e)** Calculated frontier orbitals involved in the TLS and the proposed transition state of C–H activation step. HOMO highest occupied molecular orbital, LUMO lowest unoccupied molecular orbital. *Designated when considering spin–orbital coupling, equivalent to singly occupied molecular orbital (SOMO) in restricted formalism.

oxo[21]. We measured **1**'s optical absorption (Supplementary Fig. 9a) and the ^{51}V-NMR spectrum (Supplementary Fig. 9b), which confirmed that **1** is different from monometallic VO_2^+ species in an aqueous medium. Density functional theory (DFT) calculations suggest that **1** may exist as two isomers, **1a** and **1b** (Fig. 4a), with a calculated energy difference of 1.2 kcal mol^{-1}. In an attempt to obtain the correct structure of **1** and real conformation in solution, X-ray absorption spectroscopy of V atom was conducted for 10 mM **1** in 98% H_2SO_4, solid V_2O_5, and metallic V foil (solid red, dashed blue, and dashed yellow in Fig. 4b, c, respectively). We carried out a least-square-regression analysis on X-ray absorption near-edge structure (XANES) for the threshold positions, the first peak in the derivative spectra, of VO, V_2O_3, VO_2, and V_2O_5 to determine the electronic structure and oxidation state of vanadium in **1** (Supplementary Fig. 9c)31. The electronic structure of vanadium in **1** remains similar to that of vanadium in V_2O_5, confirming the d^0 electronic structure of vanadium. The extended X-ray absorption fine structure (EXAFS) can offer coordination information of absorbing atoms by extracting the structural parameters. As shown in Fig. 4c, the absence of noticeable peaks in the region beyond 4 Å (solid red), compared with those of V_2O_5 and V foil (dashed blue and dashed yellow, respectively), indicates

that **1** is a complex homogenously dispersed in the solvent. The peak around 1.56 Å in **1**'s EXAFS spectrum (gray area) is attributed to the V–O bonds, following the assignment of V–O bonds in the V_2O_5 sample. While this comparison provides some information, the general low symmetries of the vanadium-based species prevent us from gaining detailed structural information of **1** solely based on EXAFS data[32]. To this end, we conducted the fitting of **1**'s V K-edge EXAFS spectrum combining the structure suggested by DFT calculations (shown in Fig. 4d). It reveals that the central V atoms are penta-coordinated by O atoms with three types of V–O bond lengths (1.58, 1.68, and 1.96 Å) in the first coordinated shell, with a bridging oxo with a V–O bond length of 1.68 Å. We note that the EXAFS of **1** suggests a unique coordination environment 2.0–3.5 Å away from V atom (blue area), which is different from the monometallic VO_2^+ species in aqueous medium (Supplementary Fig. 9d). The fitting results of second shell (blue area) indicate that consistent with the predicted structure **1a**, there are not only three S atoms in the second shell (2.73 and 3.13 Å) but also one V atom at the distance of 3.27 Å away from the central V atom (Supplementary Table 3). Detailed analysis is provided in the Supplementary information (Supplementary Fig. 9e, f). These results reveal the existence of a hypothesized structure of μ-oxo bridged $V_2^{V,V}$ dimer[33], and suggest that **1a** is the structure of **1** in the solution.

Additional operando characterizations were conducted to confirm a homogenous electrocatalysis and elucidate identities of immediate species. Operando Raman spectroscopy measures the vibrational spectra of chemical species near the FTO electrode at different values of E in CH_4. No spectral changes were observed and the vibrational spectra evidently differs from solid V_2O_5 sample (Supplementary Fig. 10). This suggests that there is no detectable heterogeneous intermediate deposited on the FTO electrode during electrocatalysis. Operando XAS spectra of V

atom was also measured at different values of E in CH_4. Largely, the XANES and EXAFS spectra (Supplementary Figs. 11 and 12) differ from the ones of solid V_2O_5 sample and supports a homogenous electrocatalysis. Yet some information of reaction intermediates is available. The formal oxidation state of V species, indicative in the pre-edge region of XANES spectra (Supplementary Fig. 11), decreases from +5 to near +4 with increasing value of E, contrary to the typical trend observed in heterogeneous catalysts of electrochemical oxidation[34]. This reveals the presence of mixed valence $V_2^{IV,V}$ during catalysis (Supplementary Note 3). It also supports a homogenous, diffusion-controlled catalysis, since a hypothetical immobile V(IV) species deposited on the electrode may not have long enough lifetime to be detectable (Supplementary Note 3), given the large thermodynamic driving force of oxidizing V(IV) (>1.2 V from Fig. 2a). The pre-edge region also witnesses a broadening and intensity decrease of the pre-edge peak concurrent with the increase of E and the observation of electrocatalytic CH_4 functionalization (Supplementary Fig. 11). This suggests an increase of coordination symmetry near V atom and possibly a loss of sulfonic ligand[31]. The operando EXAFS results (Supplementary Fig. 12) also displays a decrease of average coordination number of sulfonic ligands per V atom concurrent with increasing E values. Those results imply that the bisulfate group in CH_3OSO_3H likely originate from the vanadium catalyst, a plausible radical rebound mechanism[35].

Combining experimental and computational results, we established a proposed catalytic cycle of **1** for CH_4 functionalization (Fig. 1d) despite its uncommon assignment of TLS that warrants additional investigation (Supplementary Note 2). A turnover-limiting electrochemical oxidation of **1a** removes one electron from O 2p orbitals in the sulfonic ligand, which is calculated as the highest occupied molecular orbital (HOMO) of **1a** (Fig. 4e). The resultant cation radical **2** is predicted to possess an empty frontier spin-orbital on the same O 2p orbitals (lowest unoccupied

molecular orbital (LUMO) of **2** in Fig. 4e), which is postulated to initiate H-atom abstraction from CH_4. DFT calculations predict reaction trajectory between **2** and CH_4 without significant energy barrier (Fig. 4e, Supplementary Fig. 13a). This is consistent with our experimental observation that the TLS is the one-electron oxidation of **1** other than the step of C–H activation (Supplementary Note 2). The calculated barrier-less C–H activation also helps explain the similar TOFs toward various light alkanes in the natural gas[24]. We were unable to experimentally characterize **2** and the H-atom abstraction step due to its transient nature, which will be of our research focus in the future. Yet the subsequent steps of CH_4 functionalization seems to proceed with the formation of CH_3• and a radical rebound process[35]. This leads to a two-electron oxidation and CH_3OSO_3H formation with a ligand loss on a $V_2^{IV,V}$ dimer (**3**), which will be readily re-oxidized electrochemically to regenerate **1** (Fig. 1d, Supplementary Fig. 14).

DFT calculations of the atomic charges[36] suggest that cation radical **2** is stabilized thanks to orbital delocalization, in comparison to the scenario when one electron was removed from sulfuric acid (Supplementary Fig. 13b, c). This is consistent with the results that the calculated ionization energies of **1a** is lower by 12–14 kcal mol^{-1} than that of sulfuric acid. This implies that the metal-oxo centers as carrier of sulfonic ligands stabilize the electrochemically generated cation radical, at the same time maintain a cation radical reactive enough for ambient CH_4 functionalization. Other d^0 early transition-metal-oxo species can possess similar reactivities. We found that d^0 metal-oxo species, including Ti^{IV}-oxo and Cr^{VI}-oxo, are also electrochemically active towards functionalizing CH_4 at ambient conditions (Supplementary Fig. 15). A more extensive survey over the first half of the Period 4 elements except Sc indicates that only Ti, V, Cr, and possibly Mn display similar reactivities (Supplementary Fig. 16). It suggests the strategy of employing d^0 early transition-metal-oxo species is generally applicable for ambient

electrochemical functionalization of natural gas. As such a general trend of reactivity was not observed before, we posit our electrochemical approach may offer new perspective towards the challenge of CH_4 functionalization. Practically, a heterogeneous catalyst variant may also be desirable. While **1** is characterized as a homogenous catalyst, we found a two-dimensional layered material, $VOPO_4 \cdot 2H_2O$ (**4**) with exposed V-oxo edges[37] (Supplementary Fig. 17a, b), acts as a heterogeneous variant of **1** in 98% H_2SO_4 (Supplementary Fig. 17c, d). This preliminary result suggests that even within the same metal-oxo system, the catalyst subsequently its reactivity can be tuned with additional materials design and engineering. This heterogenous variant also simplifies product separation in downstream process, thanks to the absence of vanadium in the liquid phase.

2.4 Conclusion

Overall, the general tunability of catalyst composition may herald better catalysts with higher TOF, lower oxidation potential, as well as versatile design of the overall process. The ambient condition of reported catalysis facilitates the use of O_2 in ambient air as the terminal electron acceptor, as well as the use of ambient natural gas feedstock for onsite functionalization without a centralized facility. Future research will focus on possible scale-up with the exploration of optimal reaction conditions. The employment of 98% H_2SO_4 or more diluted acids, other than oleum, mitigates the generation of excessive acid in product separation and is attractive for practical application[38]. Additional fundamental and engineering investigation, including the employment of gas diffusion electrode[39] as well as ingenious design of electrochemical reactors[28], will further explore the possible application of converting CH_4 into commodity chemicals with minimal infrastructure support at remote locations. This will lead to the more efficient usage of green-house gases and reducing their emission into atmosphere.

Data availability: All data reported or included in this analyzed during this study are included in this published article (and its supplementary information).

2.5 References

1. McFarland, E. Unconventional chemistry for unconventional natural gas. Science 338, 340–342 (2012).

2. Schüth, F. Making more from methane. Science 363, 1282–1283 (2019).

3. Periana, R. A. et al. A mercury-catalyzed, high-yield system for the oxidation of methane to methanol. Science 259, 340–343 (1993).

4. Periana, R. A. et al. Platinum catalysts for the high-yield oxidation of methane to a methanol derivative. Science 280, 560–564 (1998).

5. O'Reilly, M. E., Kim, R. S., Oh, S. & Surendranath, Y. Catalytic methane monofunctionalization by an electrogenerated high-valent Pd intermediate. ACS Cent. Sci. 3, 1174–1179 (2017).

6. Kim, R. S. & Surendranath, Y. Electrochemical reoxidation enables continuous methane-to-methanol catalysis with aqueous Pt salts. ACS Cent. Sci. 5, 1179–1186 (2019).

7. Shan, J. J., Li, M. W., Allard, L. F., Lee, S. S. & Flytzani-Stephanopoulos, M. Mild oxidation of methane to methanol or acetic acid on supported isolated rhodium catalysts. Nature 551, 605–608 (2017).

8. Mukhopadhyay, S. & Bell, A. T. A high-yield approach to the sulfonation of methane to methanesulfonic acid initiated by H_2O_2 and a metal chloride. Angew. Chem. Int. Ed. 42, 2990–2993 (2003).

9. Basickes, N., Hogan, T. E. & Sen, A. Radical-initiated functionalization of methane and ethane in fuming sulfuric acid. J. Am. Chem. Soc. 118, 13111–13112 (1996).

10. Nizova, G. V., SussFink, G. & Shulpin, G. B. Catalytic oxidation of methane to methyl hydroperoxide and other oxygenates under mild conditions. Chem. Commun. 397–398 (1997).

11. Gunsalus, N. J. et al. Homogeneous functionalization of methane. Chem. Rev. 117, 8521–8573 (2017).

12. Shilov, A. E. & Shul'pin, G. B. Activation of C-H bonds by metal complexes. Chem. Rev. 97, 2879–2932 (1997).

13. Meng, X. G. et al. Direct methane conversion under mild condition by thermo-, electro-, or photocatalysis. Chem 5, 2296–2325 (2019).

14. Zimmermann, T., Soorholtz, M., Bilke, M. & Schüth, F. Selective methane oxidation catalyzed by platinum salts in oleum at turnover frequencies of large-scale industrial processes. J. Am. Chem. Soc. 138, 12395–12400 (2016).

15. Díaz-Urrutia, C. & Ott, T. Activation of methane to CH_3^+: a selective industrial route to methanesulfonic acid. Science 363, 1326–1329 (2019).

16. Labinger, J. A. & Bercaw, J. E. Understanding and exploiting C-H bond activation. Nature 417, 507–514 (2002).

17. Olah, G. A. Electrophilic methane conversion. Acc. Chem. Res. 20, 422–428 (1987).

18. Shilov, A. E. & Shul'pin, G. B. Activation and Catalytic Reactions of Saturated Hydrocarbons in the Presence of Metal Complexes. (Springer, Dordrecht, 2000).

19. Saveant, J. M.́ Elements of Molecular and Biomolecular Electrochemistry. An Electrochemical Approach to Electron Transfer Chemistry. (Wiley, New Jersey, 2006).

20. Sauermann, N., Meyer, T. H., Qiu, Y. A. & Ackermann, L. Electrocatalytic C-H activation. ACS Catal. 8, 7086–7103 (2018).

21. Madic, C., Begun, G. M., Hahn, R. L., Launay, J. P. & Thiessen, W. E. Dimerization of aquadioxovanadium(V) ion in concentrated perchloric and sulfuric-acid media. Inorg. Chem. 23, 469–476 (1984).

22. Zanello, P. Inorganic Electrochemistry: Theory, Practice and Application. (Royal Society of Chemistry, London, 2003).

23. Costentin, C., Drouet, S., Robert, M. & Saveant, J. M. Turnover numbers, turnover frequencies, and overpotential in molecular catalysis of electrochemical reactions. Cyclic voltammetry and preparative-scale electrolysis. J. Am. Chem. Soc. 134, 11235–11242 (2012).

24. Labinger, J. A. Selective alkane oxidation: hot and cold approaches to a hot problem. J. Mol. Catal. A 220, 27–35 (2004).

25. Konnick, M. M. et al. A mechanistic change results in 100 times faster C-H functionalization for ethane versus methane by a homogeneous Pt catalyst. J. Am. Chem. Soc. 136, 10085–10094 (2014).

26. Natural Gas Safety Data Sheet by SoCalGas. https://www.socalgas.com/ documents/safety/safety-data-sheet-natural-gas.pdf.

27. Dinh, C. T., Li, Y. G. C. & Sargent, E. H. Boosting the single-pass conversion for renewable chemical electrosynthesis. Joule 3, 13–15 (2019).

28. Ripatti, D. S., Veltman, T. R. & Kanan, M. W. Carbon monoxide gas diffusion electrolysis that produces concentrated C_2 products with high single-pass conversion. Joule 3, 240–256 (2019).

29. Zhu, J., Hii, K. K. & Hellgardt, K. Toward a green generation of oxidant on demand: practical electrosynthesis of ammonium persulfate. ACS Sustain. Chem. Eng. 4, 2027–2036 (2016).

30. Radimer, K. J. & McCarthy, M. J. Electrolytic Production of Sodium Persulfate. USA patent US 4,144,144 (1979).

31. Wong, J., Lytle, F. W., Messmer, R. P. & Maylotte, D. H. K-edge absorption spectra of selected vanadium compounds. Phys. Rev. B 30, 5596–5610 (1984).

32. Bunker, G. Introduction to XAFS: A Practical Guide to X-Ray Absorption Fine Structure Spectroscopy. (Cambridge University Press, Cambridge, 2010).

33. Yamada, S., Katayama, C., Tanaka, J. & Tanaka, M. Molecular structure of (u-oxo)bis[oxobis(8-quinolinolato)vanadium(V)]. Inorg. Chem. 23, 253–255 (1984).

34. Bai, L. C., Hsu, C. S., Alexander, D. T. L., Chen, H. M. & Hu, X. L. A cobalt-iron double-atom catalyst for the oxygen evolution reaction. J. Am. Chem. Soc. 141, 14190–14199 (2019).

35. Huang, X. Y. & Groves, J. T. Beyond ferryl-mediated hydroxylation: 40 years of the rebound mechanism and C-H activation. J. Biol. Inorg. Chem. 22, 185–207 (2017).

36. Reed, A. E., Weinstock, R. B. & Weinhold, F. Natural population analysis. J. Chem. Phys. 83, 735–746 (1985).

37. Wu, C. Z. et al. Two-dimensional vanadyl phosphate ultrathin nanosheets for high energy density and flexible pseudocapacitors. Nat. Commun. 4, 2431 (2013).

38. Michalkiewicz, B., Ziebro, J. & Tomaszewska, M. Preliminary investigation of low-pressure membrane distillation of methyl bisulphate from its solutions in fuming sulphuric acid combined with hydrolysis to methanol. J. Membr. Sci. 286, 223–227 (2006).

39. Higgins, D., Hahn, C., Xiang, C. X., Jaramillo, T. F. & Weber, A. Z. Gas-diffusion electrodes for carbon dioxide reduction: a new paradigm. ACS Energy Lett. 4, 317–324 (2019).

40. Yamamoto, N., Hiyoshi, N. & Okuhara, T. Thin-layered sheets of $VOHPO_4$. $0.5H_2O$ prepared from $VOPO_4$. $2H_2O$ by intercalation-exfoliation-reduction in alcohol. Chem. Mater. 14, 3882–3888 (2002).

41. Young, M. E., Carroad, P. A. & Bell, R. L. Estimation of diffusion-coefficients of proteins. Biotechnol. Bioeng. 22, 947–955 (1980).

42. Ahlrichs, R., Bar, M., Haser, M., Horn, H. & Kolmel, C. Electronic-structure calculations on workstation computers—the program system turbomole. Chem. Phys. Lett. 162, 165–169 (1989).

43. Haser, M. & Ahlrichs, R. Improvements on the direct SCF method. J. Comput. Chem. 10, 104–111 (1989).

44. Treutler, O. & Ahlrichs, R. Efficient molecular numerical-integration schemes. J. Chem. Phys. 102, 346–354 (1995). 45. Eichkorn, K., Weigend, F., Treutler, O. & Ahlrichs, R. Auxiliary

basis sets for main row atoms and transition metals and their use to approximate Coulomb potentials. Theor. Chem. Acc. 97, 119–124 (1997).

46. Eichkorn, K., Treutler, O., Ohm, H., Haser, M. & Ahlrichs, R. Auxiliary basis-sets to approximate Coulomb potentials. Chem. Phys. Lett. 242, 652–660 (1995). 47. Weigend, F. Accurate Coulomb-fitting basis sets for H to Rn. Phys. Chem. Chem. Phys. 8, 1057–1065 (2006).

48. Sierka, M., Hogekamp, A. & Ahlrichs, R. Fast evaluation of the Coulomb potential for electron densities using multipole accelerated resolution of identity approximation. J. Chem. Phys. 118, 9136–9148 (2003).

49. Deglmann, P., May, K., Furche, F. & Ahlrichs, R. Nuclear second analytical derivative calculations using auxiliary basis set expansions. Chem. Phys. Lett. 384, 103–107 (2004).

50. Arnim, M. V. & Ahlrichs, R. Parallelization of density functional and RI-Coulomb approximation in turbomole. J. Comp. Chem. 19, 1746–1757 (1998).

51. von Arnim, M. & Ahlrichs, R. Geometry optimization in generalized natural internal coordinates. J. Chem. Phys. 111, 9183–9190 (1999).

52. Ahlrichs, R. Efficient evaluation of three-center two-electron integrals over Gaussian functions. Phys. Chem. Chem. Phys. 6, 5119–5121 (2004).

53. Zhao, Y. & Truhlar, D. G. The M06 suite of density functionals for main group thermochemistry, thermochemical kinetics, noncovalent interactions, excited states, and transition elements: two new functionals and systematic testing of four M06-class functionals and 12 other functionals. Theor. Chem. Acc. 120, 215–241 (2008).

54. Weigend, F. & Ahlrichs, R. Balanced basis sets of split valence, triple zeta valence and quadruple zeta valence quality for H to Rn: Design and assessment of accuracy. Phys. Chem. Chem. Phys. 7, 3297–3305 (2005).

55. Klamt, A. & Schuurmann, G. Cosmo—a new approach to dielectric screening in solvents with explicit expressions for the screening energy and its gradient. J. Chem. Soc. Perkin Trans. 2, 799–805 (1993).

56. Gillespie, R. J. & Cole, R. H. The dielectric constant of sulphuric acid. Trans. Faraday Soc. 52, 1325–1331 (1956).

Supplementary references

1. Madic, C., Begun, G. M., Hahn, R. L., Launay, J. P. & Thiessen, W. E. Dimerization of aquadioxovanadium(V) ion in concentrated perchloric and sulfuric-acid media. Inorg. Chem. 23, 469-476, (1984).

2. Díaz-Urrutia, C. & Ott, T. Activation of methane to CH_3^+ : a selective industrial route to methanesulfonic acid. Science 363, 1326-1329, (2019).

3. Sadow, A. D. & Tilley, T. D. Homogeneous catalysis with methane. A strategy for the hydromethylation of olefins based on the nondegenerate exchange of alkyl groups and sigma-bond metathesis at scandium. J. Am. Chem. Soc. 125, 7971-7977, (2003).

4. Meyer, D. et al. Palladium complexes with pyrimidine-functionalized N-heterocyclic carbene ligands: synthesis, structure and catalytic activity. Organometallics 28, 2142- 2149, (2009).

5. O'Reilly, M. E., Kim, R. S., Oh, S. & Surendranath, Y. Catalytic methane monofunctionalization by an electrogenerated high-valent Pd intermediate. ACS Cent. Sci. 3, 1174-1179, (2017).

6. Kim, R. S. & Surendranath, Y. Electrochemical reoxidation enables continuous methane-to-methanol catalysis with aqueous Pt salts. ACS Cent. Sci. 5, 1179-1186, (2019).

7. Chan, S. I. et al. Efficient oxidation of methane to methanol by dioxygen mediated by tricopper clusters. Angew. Chem. Int. Ed. 52, 3731-3735, (2013).

8. Periana, R. A. et al. A mercury-catalyzed, high-yield system for the oxidation of methane to methanol. Science 259, 340-343, (1993).

9. Periana, R. A., Mironov, O., Taube, D., Bhalla, G. & Jones, C. J. Catalytic, oxidative condensation of CH_4 to CH_3COOH in one step via CH activation. Science 301, 814- 818, (2003).

10. Jones, C. J. et al. Selective oxidation of methane to methanol catalyzed, with C-H activation, by homogeneous, cationic gold. Angew. Chem. Int. Ed. 43, 4626-4629, (2004).

11. Smith, K. T. et al. Catalytic borylation of methane. Science 351, 1424-1427, (2016).

12. Periana, R. A. et al. Platinum catalysts for the high-yield oxidation of methane to a methanol derivative. Science 280, 560-564, (1998).

13. Hu, A. H., Guo, J. J., Pan, H. & Zuo, Z. W. Selective functionalization of methane, ethane, and higher alkanes by cerium photocatalysis. Science 361, 668-672, (2018).

14. Zimmermann, T., Soorholtz, M., Bilke, M. & Schüth, F. Selective methane oxidation catalyzed by platinum salts in oleum at turnover frequencies of large-scale industrial processes. J. Am. Chem. Soc. 138, 12395-12400, (2016).

15. Munz, D., Meyer, D. & Strassner, T. Methane CH activation by palladium complexes with chelating bis(NHC) ligands: a DFT study. Organometallics 32, 3469-3480, (2013).

16. Fuller, J. T. et al. Catalytic mechanism and efficiency of methane oxidation by Hg(II) in sulfuric acid and comparison to radical initiated conditions. ACS Catal. 6, 4312- 4322, (2016).

17. Chempath, S. & Bell, A. T. Density functional theory analysis of the reaction pathway for methane oxidation to acetic acid catalyzed by Pd^{2+} in sulfuric acid. J. Am. Chem. Soc. 128, 4650-4657, (2006).

18. Mironov, O. A. et al. Using reduced catalysts for oxidation reactions: mechanistic studies of the "Periana-Catalytica" system for CH_4 oxidation. J. Am. Chem. Soc. 135, 14644-14658, (2013).

19. Costentin, C., Drouet, S., Robert, M. & Saveant, J. M. Turnover numbers, turnover frequencies, and overpotential in molecular catalysis of electrochemical reactions. Cyclic voltammetry and preparative-scale electrolysis. J. Am. Chem. Soc. 134, 11235- 11242, (2012).

20. Savéant, J. M. Elements of molecular and biomolecular electrochemistry. An electrochemical approach to electron transfer chemistry. (Wiley, New Jersey, 2006).

21. Bolton, J. R. & Archer, M. D. Electron transfer in inorganic, organic, and biological systems. Chapter 2, pp 7-23. Basic electron-transfer theory. (The American Chemical Society, 1991).

22. Robertson, J. Electronic structure of SnO2, GeO2, PbO2, TeO2 and MgF2. J. Phys. C: Solid State Phy. 12, 4767-4776, (1979).

23. Hanna, C. M., Sanborn, C. D., Ardo, S. & Yang, J. Y. Interfacial electron transfer of ferrocene immobilized onto indium tin oxide through covalent and noncovalent interactions. Acs Appl. Mater. Interfaces 10, 13211-13217, (2018).

24. Hamann, T. W., Farha, O. K. & Hupp, J. T. Outer-sphere redox couples as shuttles in dye-sensitized solar cells. Performance enhancement based on photoelectrode modification via atomic layer deposition. J. Phys. Chem. C 112, 19756-19764, (2008).

25. Bai, L. C., Hsu, C. S., Alexander, D. T. L., Chen, H. M. & Hu, X. L. A cobalt-iron double-atom catalyst for the oxygen evolution reaction. J. Am. Chem. Soc. 141, 14190- 14199, (2019).

26. Lin, F. et al. Synchrotron X-ray analytical techniques for studying materials electrochemistry in rechargeable batteries. Chem. Rev. 117, 13123-13186, (2017).

CHAPTER 3: Electrocatalytic oxidation of methane to methyl hydrogen sulfate with molecular transition metal silver species

This chapter is a version of: D. Xiang, J. A. Iñiguez, J. Deng, X. Guan, A. Martinez, C. Liu, *Angew. Chem. Int. Ed.* 2021, *60*, 18152.

3.1 Introduction

Ambient CH_4 functionalization offers a route of chemical synthesis that taps on the vast, widely distributed natural gas resources while mitigating the environmentally unfriendly CH_4 emission into the atmosphere[1]. The key step in this process is the activation of CH_4's C-H bond at relatively low temperature and pressure, which demands a kinetically reactive species with a low activation barrier[2]. One approach in search of the desirable reactive species begins from the classic hard-soft acid-base (HSAB) theory, initially introduced by Ralph Pearson[3]. The theory introduces chemical hardness η as a measure of molecules' electrophilicity[4] and stability in the context of Lewis acid-base adduct. In a homolytic cleavage of CH_4 , the transferred methyl moiety possesses relatively low chemical hardness ($\eta = 4.87$).[5] The softness of methyl moiety along with H atom ($\eta = 6.42$) involved in H-atom abstraction suggests that a soft, class (b) transition-metal Lewis acid of high valence and increased electrophilicity may be reactive towards CH_4 via either electrophilic activation[6] or a radical-based mechanism.[7] Consistently, many high-valent class (b) metals in the d-block of periodic table, including $Rh^{I,II}$,[8] $Pd^{II,III}$,[9] Ir^{III} ,[10] $Pt^{II,IV}$,[11] $Au^{I,III}$,[12] Hg^{II} , [6b] have been reported for CH_4 activation (Figure 1 a). Some of the borderline metals with intermediate chemical softness, including Mn^{III} ,[13] Co^{III} ,[13] $Ru^{IV,VIII}$,[14] $Os^{IV,VIII}$,[15] Tl^{III} ,[6c] and Pb^{IV} ,[6c,13] are reactive towards CH_4 , too. Yet there is one exception, silver

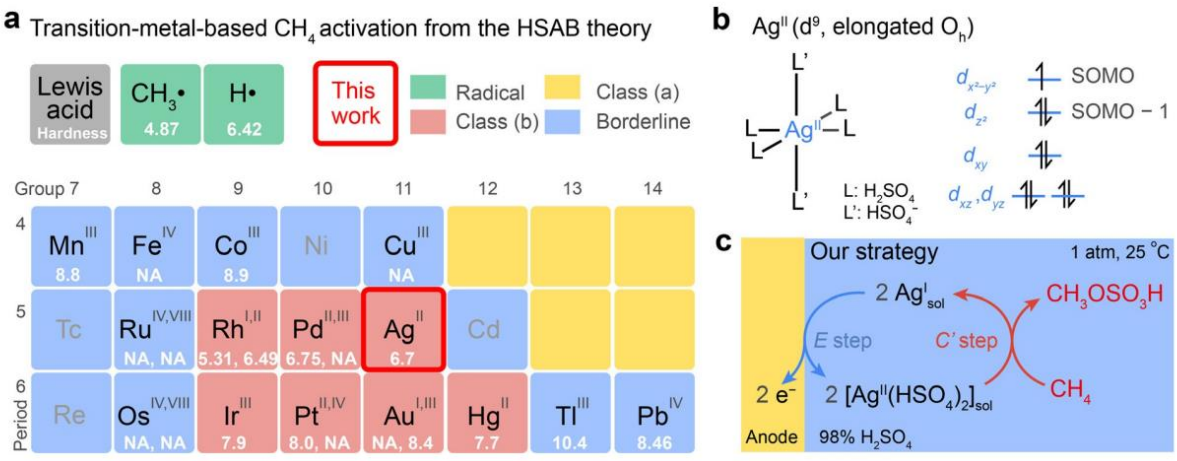

Figure 3.1: a) Transition metals reported for direct C—H activation of homogeneous CH_4 functionalization.[2b] The values of chemical hardness (η) are tabulated for the elements' respective oxidation states.[5] NA, not available. b) The frontier orbitals and structure of a proposed Ag^{II} metalloradical in 98% H_2SO_4 . L and L', ligands; SOMO, Singly Occupied Molecular Orbital. c) The strategy of an electrocatalytic CH_4 activation in this work.

(Ag). While monovalent Ag^I as a mild oxidant (η = 6.96; E^o = 0.80 V vs. normal hydrogen electrode (NHE) for Ag^+ (aq.)/Ag (s))[5, 16] may not be oxidative enough to break the C-H bond in CH_4 (E^o = 0.59 V vs. NHE for CH_3OH (l)/CH_4 (g)),[2b, 16] divalent Ag^{II} is similarly soft (η = 6.7)[5] and possesses a Ag^{II}/Ag^I redox potential ($E^o \approx$ 2.5 V vs. NHE for Ag^{II}/Ag^I in 98% H_2SO_4)[17] comparable to other reported CH_4 -activation catalysts. [2a,b, 9b] Therefore, it is intriguing that divalent Ag^{II} has not been known for CH_4 activation despite the reported Ag^{II}-based reactivities on much weaker C-H bonds in organic synthesis. [18] The d^9 electronic configuration of Ag^{II} not only renders it a metalloradical, but also introduces the Jahn–Teller effect in an O_h ligand field that elongates the ligand bond in the axial position (Figure 1 b).[19] Such weakly bound axial ligands and Ag^{II} 's likely radical nature may offer an opportunity for substrate binding and CH_4

activation in a radical-based activation pathway with low reaction barrier, leading to our hypothesis that Ag^{II}, once continuously generated, may serve as the active species towards ambient CH_4 functionalization catalytically.

Our strategy of investigating Ag^{II} as a potential active species towards CH_4 activation includes continuous electrogeneration of reactive Ag^{II} species in an inert solvent environment (Figure 1 c). Electrochemistry offers a viable and clean route of creating reactive intermediates for synthesis including C-H activation.[20] Such a strategy has enabled our previous discovery of electrocatalytic CH_4 functionalization with vanadium-oxo dimer as the homogeneous catalysts at ambient temperature and pressure. [2a] Similarly, the strategy of electrochemical catalysis can be also applied for the generation of Ag^{II} intermediate, which circumvents the instability of Ag^{II} and establishes an electrocatalytic cycle mediated by the Ag^{II}/Ag^{I} redox couple (Figure 1 c). We also sought to choose a weakly bound solvation environment as a model system that offers labile binding sites for substrate activation, supports the radical nature of Ag^{II} in a possible radical-based mechanism, and mitigates side reactions of solvent oxidation due to Ag^{II}'s reactive nature. Such consideration leads to the choice of 98% H_2SO_4 , which not only minimizes possible water oxidation reaction due to its oxidative stability[2a,b] but also can stabilize Ag^{II} compound at 208 ^{o} C.[21] The electron-withdrawing bisulfate ligand bound to Ag^{II} in 98% H_2SO_4 is postulated to provide access to CH_4 activation in the elongated axial position,[19a] maximize the radical nature on metal center due to spin localization,[19b] and simplify product detection by mitigating the additional oxidation with the formation of methyl bisulfate (CH_3OSO_3H) after a presumed two-electron oxidation. Such favorable features in conjunction with our expertise in electrochemical CH_4 activation[2a, 22] constitute our motivation for exploring a Ag^{II}-mediated electrocatalytic CH_4 functionalization in 98% H_2SO_4 inspired by the HSAB theory.

Here we present our demonstration of Ag^{II}-mediated electrocatalytic CH_4 activation in 98% H_2SO_4 at ambient conditions. We found that electrochemically generated Ag^{II} intermediate is capable of activating CH_4 and yielding CH_3OSO_3H with minimal side reactions at room temperature and ambient pressure. The CH_4 -activation reactivity, measured as the partial current density of CH_3OSO_3H formation j_{CH4} , is systematically studied as a function of the applied electrochemical potential (E), duration of electrolysis (t), the concentration of pre-catalyst Ag^I (c_{Ag}), temperature (T), and the partial pressure of CH_4 (p_{CH4}) up to 125 psi. The results support the scheme of electrocatalysis for CH_4 functionalization mediated by Ag^{II} in an EC' mechanism[23] (Figure 1 c), in which the electrochemically generated Ag^{II} undergoes a turnover-limiting CH_4 -activating step with low activation energy (13.1 kcal mol^{-1}), high pseudo-first-order rate constant (k_{obs}) of 2.8 x 10^3 h^{-1} (p_{CH4} = 85 psi), and a high turnover number (TON) of about 2.45 x 10^4 when t = 72 h and p_{CH4} = 125 psi. Three independent kinetic characterizations suggest that Ag^{II}-mediated CH_4 activation is kinetically favored at room temperature over the side reaction of solvent oxidation. The overall selectivity of the reaction, measured as the Faradaic efficiency (FE) in electrocatalysis, was observed to be 72% when p_{CH4} = 85 psi and is predicted to exceeding 99% when p_{CH4} > 180 psi after overcoming the mass-transport constraint due to CH_4's limited solubility. The discovered reactivity of electrochemically generated Ag^{II}, in conjunction with Ag's relatively lower cost comparing to its more precious counterparts in class (b) metals (Hg notwithstanding), offer a favorable prospect for its utilization in chemical production from widely distributed natural gas with minimal infrastructure reliance.

3.2 Experimental

Chemicals and materials

All reagents were used without further purification unless otherwise specified and were obtained from Sigma-Aldrich, Inc., Thermo Fisher Scientific, Inc., or VWR International, LLC. Dimethyl sulfoxide-D6 (D, 99.9%) was attained from Cambridge Isotope Laboratories, Inc. Deionized (DI) water (18 MΩ cm−1 resistivity) was produced from the Milli-Q Water Purification System of Millipore. Chemically pure (CP) grade CH4 (Min. Purity 99.5%) and ultra-high-purity (UHP) grade N2 (Min. Purity 99.999%) were supplied by Airgas, Inc. ^{13}C labeled methane ($^{13}CH4$ 99%; 99 atom% ^{13}C) was purchased from the Sigma-Aldrich.

Chemical characterizations

Ultraviolet-visible (UV-Vis) spectra at room temperature were processed through Agilent Cary 60 UV-Vis spectrophotometer. Temperature-dependent UV-Vis spectra were obtained by JASCO V770 UV-Visible/NIR spectrophotometer with accessory ETCS-761. ^{1}H-NMR and ^{13}C NMR spectra were recorded on Bruker Avance spectrometer (400 MHz). Electron paramagnetic resonance (EPR) was performed on a Bruker EMX X-band continuous-wave (CW) EPR spectrometer. The products in the gas phase were detected online by an SRI multiple gas analyzer #5 gas chromatograph (GC), 8610C, fabricated with 3 S.S. columns including one 18" Hayesep D, one 3'MS 5A, and one 6' Hayesep D.

Catalyst preparation

Complex Ag^{I} sol, serving as the precatalyst Ag^{I} in the liquid phase, was prepared by dissolving silver (I) sulfate ($Ag^{I}_2SO_4$) and sonicating in 98% H_2SO_4 with 2 h, and the corresponding solution was used as the working solution in bulk electrolysis. c_{Ag}, the bulk concentration of the

precatalyst Ag^{I} . Complex $[Ag^{II}(HSO_4)_2]$sol, serving as the active Ag^{II} species, was in situ electrogenerated from Ag^{I} at the anode (see the insets in Figure S2).

Electrochemical characterizations

All electrochemical experiments were recorded using Gamry Instruments Interface 1000E potentiostat. Fluorine-Tin-Oxide (FTO) Coated Glass Plates (TEC7) were purchased from Hartford Glass, Inc. Other electrodes were purchased from CH Instruments, Inc. unless otherwise indicated. A three-electrode setup was applied with an FTO glass working electrode, a Ag wire pseudo-reference electrode and a Pt wire counter electrode (Figure S5). The FTO working electrode was manufactured by connecting tungsten wire (0.01" diameter) to it and binding Teflon tapes so that the exposed surface area was 1 cm × 1 cm. The Ag wire pseudo-reference electrode was fabricated by dipping the Ag wire into a Ag_2SO_4 (98% H_2SO_4) solution in a glass tubing sealed with a porous tip. The Ag^{I} solution in the glass tubing had the same c_{Ag} as the working solution used in bulk electrolysis. The Ag wire pseudo-reference electrode was calibrated to a Hg_2SO_4/Hg (saturated K_2SO_4) reference electrode by measurement of open-circuit potential (OCP). The conversion is E (V vs Hg_2SO_4/Hg) = E (V vs Ag) + OCP, where the OCP value is dependent on c_{Ag} (for c_{Ag} = 0.1 mM, OCP ~ −340 mV vs Hg_2SO_4/Hg; for c_{Ag} = 10 mM, OCP ~ −270 mV vs Hg_2SO_4/Hg). The working solution was saturated by continuously bubbling N_2 or CH_4 into the cell with the use of a mass flow controller acquired from Omega Engineering, Inc. FMA5510A. iR compensation was conducted for all measurements. The experiments at elevated absolute pressures of CH_4 (p_{CH4}) was conducted by inserting the electrochemical cell into a custom-designed setup composed of a pressure vessel with two gas tubings and three electric feedthroughs (Parr Instrument, Series 4600, 1000 mL) (Figure S1). In this setup, p_{CH4}

was controlled between 0 and 165 psi, and a constant gas flow was maintained by the mass flow controller during the electrolysis.

Cyclic voltammetry

CV data were recorded using an FTO working electrode, a Ag wire pseudoreference electrode, and a Pt wire counter electrode. A 4 mL solution of c_{Ag} = 10 mM in 98% H_2SO_4 was placed in a single chamber and sealed in the high-pressure reactor. The working solution was first saturated by bubbling N_2 for 20 min with the assistance of stirring (150 rpm) to ensure no O_2 remained in the solution. CV data were then recorded in elevated p_{CH4} with various scan rates (v). Based on the Randles–Sevcik equation, the diffusion coefficient of the electroactive species (D) was calculated from the anodic peak current densities ($j_{p,a}$) at various scan rates in N_2 (p_{CH4} = 0) (see Figure 2b in the main text). When elevating p_{CH4}, the system was allowed to equilibrate at each p_{CH4} for 20 min before scanning the CV curves. A series of CVs were thus collected covering various p_{CH4} (from 0 to 165 psi) with different scan rates (from 5 to 1000 mV/s) and iR-compensated (Figure S4). Numerical simulations of the cyclic voltammograms when c_{Ag} = 10 mM in N_2 were conducted with DigiElch 8 Professional. The detailed parameters are shown in Table S1 and S2

Bulk electrolysis

A 1 mL sample of the pre-electrolyzed solution was reserved for the following product analysis. A 5 mL solution of Ag^I in 98% H_2SO_4 was placed in each chamber of an H-cell, where a Nafion 117 membrane was used as the separator, an FTO glass slide as the working electrode, an Ag wire as the pseudo-reference electrode, and a Pt wire as the counter electrode (Figure S5). The H-cell was then inserted into the high-pressure reactor. The working solution was first saturated

by bubbling atmospheric N_2 (p_{CH4} = 0) with a flow rate of 10 standard cubic centimeters per minute (sccm) to ensure no O_2 remained in the solution. Chronoamperometry was conducted for 3 h, meanwhile, CH_4 was bubbled into the solution with the assistance of stirring (150 rpm). The flow rate of CH_4 was 7.2 sccm if p_{CH4} = 15 psi (1 atm), or several tens of standard cubic centimeters per minute if p_{CH4} elevated. Note that the pressure should be equilibrated for 20 min before electrolysis, especially for the reaction under high p_{CH4}. The post-electrolyzed solution was analyzed by ^{1}H-NMR spectroscopy and compared with the pre-electrolyzed solution (see Figure 3a in the main text and Figure S6a).

Double potential step chronoamperometry

A 4 mL solution of c_{Ag} = 10 mM in 98% H_2SO_4 was placed in a single chamber and sealed in the high-pressure reactor. The pressure-dependent chronoamperometry was conducted with the applied potential E_1 = 2.0 V vs Hg_2SO_4/Hg for 40 s followed by E_2 = 0.75 V vs Hg_2SO_4/Hg for another 40 s (0.1 s as a sample period). The system was allowed to equilibrate at each p_{CH4} for 20 min before the chronoamperometry. The observed rate constants ($k_{obs,t}$) and turnover frequencies (TOFs) were then derived from fitting the linear region of $j(t)/j_0(t)$ vs $t^{1/2}$, where $j_0(t)$ is the current density of p_{CH4} = 0, $j(t)$ is the one of $p_{CH4} \neq 0$, $j(t)/j_0(t)$ is the normalized current density, and t is time (see Figure 6 in the main text and Table S11).

Product analysis

Characterization and quantification of liquid products: After 3 h product accumulation, quantitative ^{1}H-NMR was conducted to analyze the products in the liquid phase. The NMR sample was prepared by mixing a 0.4 mL aliquot of the post-electrolyzed solution with 0.1 mL d_6-DMSO, in which acetic acid (AcOH) was used as the internal standard. The mixed NMR

sample contained 1 mM AcOH. A working curve was plotted by calibrating the linearity of the concentration of methyl bisulfate (c_{MHS}) and its relative peak area with respect to AcOH (Figure S6d). Here, chemical shift (δ) was expressed in parts per million (ppm). When using electrolytes of 98% H_2SO_4, a singlet peak at 3.34 ppm was assigned to methyl bisulfate (MHS) with two satellite peaks appearing on either side of the main peak, whereas the singlet peak at 1.96 ppm was assigned to AcOH. No liquid products other than MHS were observed in 98% H_2SO_4. When using electrolytes of oleum (referring to the solution of sulfur trioxide in sulfuric acid, 20% free SO_3 basis), another product in the liquid phase, methane sulfonic acid (MSA), was observed after electrolysis (Figure S6c).

Solubility estimation

The singlet peak at −0.47 ppm in ^{1}H-NMR spectrum was assigned to CH_4 in 98% H_2SO_4. We observed the concentration of CH_4 in post-electrolyzed solution in the atmosphere on the order of 0.1−1 mM by ^{1}H-NMR. However, it is very difficult to accurately measure the solubility of CH_4 in liquids under a specific reaction condition due to some complicated behaviors.[1] Here we used the reported CH_4 concentration in aqueous solution at steady state[2] to estimate the order of CH_4 solubility under different pressures according to Henry's law. The CH_4 solubility in aqueous solution was estimated to be 9 mM under 165 psi CH_4 and 0.8 mM under 15 psi CH_4 in aqueous solution. Even though water and 98% H_2SO_4 are both protic media, the CH_4 solubility in 98% H_2SO_4 should be lower than the one in an aqueous solution due to the polarity difference of solvent.

Detection of gas products

Gas chromatographs were collected online by a thermal-conductivity detector (TCD) and a flame-ionization detector (FID) (with a methanizer). The outlet gas flow, together with the products from the anodic compartment, was vented directly into the sampling loop of the GC. The instrument was operated with a temperature profile from 50ºC to 270 ºC, and a flow rate of 40 mL/min at 15 psi with Ar carrier gas. Outlet gas components were analyzed before the bulk electrolysis, during the electrolysis, and at the end of the electrolysis for comparison.

Spectroscopy characterizations and analysis

Identification of the active species: A 5 mL colorless solution of c_{Ag} = 30 mM in 98% H_2SO_4 was placed in each chamber of an H-cell, where a Nafion 117 membrane was used as the separator, an FTO glass slide as the working electrode, a Ag wire as the pseudo-reference electrode, and a Pt wire as the counter electrode. After electrolysis for 30 min in N_2, the working solution became yellow while the counter solution remained colorless (see inset of Figure 3d in the main text). S7 Some dark yellow precipitates were formed at the anode due to the high local concentration of the electrogenerated Ag^{II} species. Such precipitates were tentatively assigned as $Ag^{II}(HSO_4)_2$.[3] An aliquot of the post-electrolyzed solution was immediately analyzed with UV-Vis spectroscopy at room temperature. UV-Vis spectrum was measured every 1 min to track the degradation of electrogenerated Ag^{II} species (solvent oxidation, Figure S8a). We also obtained the timedependent UV-Vis spectra of commercial AgO dissolved in 98% H_2SO_4 (Figure S8b). The similar profiles of these two solutions suggested that the post-electrolyzed solution contains the same Ag^{II} complex as the AgO solution, and henceforth the AgO solution would be referred to as the postelectrolyzed solution, of which the equivalence is noted in literature.[4] The AgO solution would then be analyzed by EPR and temperature-dependent UV-Vis spectroscopy.

EPR of Ag^{II} in 98 % H_2SO_4: EPR was performed on a Bruker EMX X-band continuous-wave (CW) EPR spectrometer. The commercial AgO was dissolved in 98 % H_2SO_4 at room temperature and transferred into the EPR tube. The solution was immediately frozen at 77 K (liquid nitrogen) and then measured by EPR. The microwave frequency was 9362.304 MHz and the power was 2 mW. The g-tensor could be converted from magnetic field by using the following equation[5] (see Figure 3e in the main text):

$$g = 0.71557 \times 9362.304\ (\text{MHz}) \div \text{Magnetic field (Gauss)}$$

Caution! The volume of 98% H_2SO_4 could expand at such low temperature, leading to the breaking of the EPR tube.

Kinetic analysis with temperature-dependent UV-Vis spectroscopy

A thermostatted cell holder was assembled to JASCO V-770 UV-Visible/NIR spectrophotometer to achieve a suitable temperature range (from 298K to 328 K). The temperature was equilibrated before scanning each spectrum. The AgO solution was freshly prepared, of which the 98% H_2SO_4 solvent was preequilibrated to a certain temperature and pre-saturated with N_2 or CH_4. The thermal decay process of Ag^{II} to Ag^{I} (solvent oxidation) at a certain temperature was tracked by monitoring the decreasing absorbance of AgO solution at 364 nm, where the blanket of N_2 gas was maintained above the solution. The overall reaction of CH_4 with Ag^{II} (CH_4 activation and solvent oxidation) at a certain temperature was monitored by measuring the absorbance of AgO solution at 364 nm, where the blanket of CH_4 was maintained above the solution and continuously supplied from the gas source outside the cell with a slow mass flow rate. Each measurement might take up to 1000~1200 s to record the complete time trace till the absorbance at 364 nm (A_{364}) dropped to zero. While the kinetic may deviate from a pseudo-first-order kinetic

on Ag^{II} at later stage of characterization due to CH_4's limited solubility, the initial kinetics of each trace were tested to be first-order kinetic as alternative reaction orders yielded unsatisfactory results (data not shown). In the following analysis, only the initial kinetic traces reflective of a pseudo-first-order kinetic on Ag^{II} were considered.

Here, we used the absorbance at 364 nm (A_{364}) to represent the concentration of reactant Ag^{II} ($[Ag^{II}]$) according to Beer-Lambert Law:

$$A_{364} = \varepsilon l[Ag^{II}]$$

where ε is the molar absorption coefficient, and l is the optical path length.

Based on the temperature-dependent decay profiles, the rate constants for chemical processes at different temperatures could be obtained by fitting the exponential rate law of (pseudo-)first-order reaction:

$$[Ag^{II}] = [Ag^{II}]0 \times e^{-kt}$$

$$A_{364} = A_{364,0} \times e^{-kt}$$

where t is time, $[Ag^{II}]_0$ is the initial concentration of Ag^{II} (t = 0), $A_{364,0}$ is the initial absorbance at 364 nm (t = 0), and k is the corresponding rate constant of (pseudo-)first-order reaction. Other kinetic equations[6] for zero-order reaction and second-order reaction have also been tested, however, giving bad fitting results.

Especially, for the pure solvent oxidation process, the kinetic equation could be represented by:

$$A_{364} = A_{364,0} \times e^{-k_{sol}t}$$

then take the natural log of both sides to obtain:

$$\ln(A_{364}) = \ln(A_{364,0}) - k_{sol}\,t$$

$$\ln(A364/A364,0) = -\,k_{sol}\,t$$

suggesting that the plot of $\ln(A_{364}/A_{364,0})$ vs t should yield a straight line with a slope of −ksol.

As for the overall reaction of CH_4 with Ag^{II}, it is composed of two parallel reactions including solvent oxidation and CH_4 activation. Their kinetics hold:

$$\text{solvent oxidation: } rate_{sol} = k_{sol}[Ag^{II}]$$

$$CH_4 \text{ activation: } rate_{CH4} = k_{CH4}\,[CH_4\,][Ag^{II}] = k_{obs,s}\,[Ag^{II}]$$

$$\text{overall reaction: } rate_{overall} = (k_{obs,s} + k_{sol})[Ag^{II}]$$

where k_{CH4} is the bimolecular rate constant of CH_4 activation, $k_{obs,s}$ is its pseudo-first-order rate constant derived from absorption spectroscopy (hence the subscript "s"), and $[CH_4]$ is the concentration of CH_4 dissolved in 98% H_2SO_4, which is on the order of 0.1−1 mM at 298 K under 15 psi according to NMR measurements.

Similarly, the kinetics of the overall reaction in CH4 could be represented by:

$$A_{364} = A_{364,0} \times e^{-(k_{obs,s}+k_{sol})t}$$

$$\ln(A_{364}/A_{364,0}) = -(k_{obs,s} + k_{sol})\,t$$

which gives the $(k_{obs,s}+k_{sol})$ value by fitting the above function of t and also gives the $k_{obs,s}$ value by ruling out k_{sol} from $(k_{obs,s}+k_{sol})$ (Table S10).

The activation energies of solvent oxidation ($E_{a,sol}$) and CH_4 activation ($E_{a,CH4}$) were directly fitted by taking the natural logarithm of the Arrhenius equation (see Figure 5f in the main text):

$$\ln(k) = -\frac{\mathrm{Ea}}{R}\left(\frac{1}{T}\right) + \ln(A)$$

where E_a is the activation energy of either solvent oxidation or CH_4 activation, R is the gas constant, T is the temperature of the experiment, and A is the pre-exponential factor. Note that the concentration of CH_4 in 98% H_2SO_4 was assumed to be a constant within the range of applied temperatures under ambient pressure.

Electrokinetic analysis

Determination of diffusion coefficient (D): As mentioned before, the diffusion coefficient for electroactive species (D) was derived from the CV curves of different scan rates.[7] Data processing was based on the Randles–Sevcik equation:

$$\text{S10}\quad j_{p,a} = 0.4463\,(nF)^{3/2}(RT)^{-1/2}c_{Ag}(vD)^{1/2}$$

where $j_{p,a}$ is the anodic peak current density, n is 1 for one-electron transferred redox process, F is the Faraday's constant, c_{Ag} is the bulk concentration of catalyst (10 mM), v is the scan rate, R is the gas constant (8.314 J mol^{-1} K^{-1}), and T is the temperature of the experiment (298 K). D was thus extracted from the slope of linear fitting of $j_{p,a}$ versus $v^{1/2}$ (Figure 2d). D is 2.8×10^{-7} $cm^2 \cdot s^{-1}$ in 98% H_2SO_4.

Determination of Faradaic efficiency (FE): To evaluate the selectivity of electrocatalyzed CH_4 functionalization, the Faradaic efficiency (FE) of bulk electrolysis was determined by the following relationship:

$$FE = \frac{nFc_{MHS}V_{electrolyes}}{Q_{overall}}\ x\ 100\%$$

where F is the Faraday's constant (96,485 C/mol), c_{MHS} is the concentration of MHS determined by quantitative ^{1}H-NMR, $V_{electrolytes}$ is the volume of working solution used in bulk electrolysis (5 mL), and the $Q_{overall}$ is the total electric charges integrated from chronoamperometry. The constant n indicates the number of transferred electrons in electrochemical reaction if one equivalent of product is formed. In this case, n is 2 for the oxidation of CH_4 to MHS.

Determination of partial current density (j_{CH4}) To evaluate the activity of electrocatalysis, the partial current density of MHS generation (j_{CH4}) was chosen to represent the reaction rate of CH4 activation. It has a relationship with total current density (j_{tot}):

$$j_{CH4} = j_{tot} \times FE$$

where FE is the Faradaic efficiency.

Determination of apparent rate constant (k_{obs}) and turnover frequency (TOF):

Method 1: See derivation of $k_{obs,s}$ in above section Kinetic analysis with temperature-dependent UV-Vis spectroscopy.

Method 2: The apparent rate constant ($k_{obs,b}$) of bulk electrolysis was calculated based on the following equation[8]:

$$k_{obs,b} = \left(\frac{j_{CH4}}{nFc_{Ag}}\right)^2 D^{-1} \quad \text{S11}$$

Method 3: The value of $k_{obs,t}$ under various p_{CH4} can be obtained from double potential step chronoamperometry (Figure 6 in the main text and Table S11). $k_{obs,t}$ at different p_{CH4} was derived by fitting the linear region of j (t)/j_0 (t) vs time$^{1/2}$ according to the following equation[9] (Figure 6b):

$$\frac{j(t)}{j_0(t)} = \sqrt{\pi k_{obs,t}}\sqrt{t}$$

where j is the current densities recorded in CH_4 ($p_{CH4} \neq 0$), j_0 is the current densities recorded in N_2 ($p_{CH4} = 0$), and t is time. Here CH_4 activation is a bimolecular reaction and its rate constant (k_{cat}) can be obtained by plotting $k_{obs,t}$ versus p_{CH4} (Figure 6c):

$$k_{obs,t} = k_{cat} \times p_{CH4}$$

and the slope gives k_{cat}.

Determination of turnover number (TON): The turnover number (TON) of each experiment was calculated from $k_{obs,b}$ according to the equation[8a, 8b]:

$$TON = \frac{n_{MHS}}{(A)(c_{Ag})}\sqrt{\frac{k_{obs,b}}{D}}$$

in which n_{MHS} is the accumulative amount of MHS, A is the area of the working electrode, c_{Ag} is the bulk concentration of the catalyst, D is the diffusion coefficient of catalyst, and $k_{obs,b}$ is the apparent rate constant. This method was employed in Figure 4b in the main text, Table S4, and Table S7.

Estimation of FE($p_{CH4, T}$): Theoretically, FE should be equal to the percentage of electrogenerated AgII involved in CH4 activation if we consider solvent oxidation as the only side reaction when estimating the achievable value of FE. Therefore, theoretical FE, as a function of pCH4 and T, can be defined by the following equation:

$$FE(p_{CH4}, T) = \frac{Rate_{CH4}}{Rate_{CH4} + Rate_{sol}}$$

considering the kinetics of CH4 activation holds:

$$rate_{CH4} = k_{CH4}(T)[CH_4][Ag^{II}]$$

and the kinetics of solvent oxidation holds:

$rate_{sol} = k_{sol}(T)[Ag^{II}]$

then FE should be equal to:

$$FE\ (p_{CH4}, T) = \frac{kCH4\ (T)[CH4\ ][AgII]}{k_{CH4}(T)[CH_4][Ag^{II}] + k_{Sol}(T)[Ag^{II}]}$$

Eliminate [AgII] from the numerator and denominator:

$$FE\ (p_{CH4}, T)\ = \frac{k_{CH4}(T)[CH_4]}{k_{CH4}CH_4\ (T)[CH_4]\ +\ k_{Sol}(T)}$$

and simplify the above equation with $k$obs($pCH4$, T) = kCH4 (T)[CH4], we get the following relationship:

$$FE\ (p_{CH4}, T)\ = \frac{k_{obs}(p_{CH4}, T)}{k_{obs}(p_{CH4}CH_4, T)\ +\ k_{sol}(T)}$$

Thanks to the well-known relationship between temperature and rate constant described by Arrhenius equation:

$$\ln\left(\frac{k_2}{k_1}\right)\ =\ -\ \frac{E_a}{R}\ \left(\frac{1}{T_2}\ -\ \frac{1}{T_1}\right)$$

and rearrange the above equation as:

$$k_2 = (k_1)\ e^{\frac{-E_a}{R}\left(\frac{1}{T_2} - \frac{1}{T_1}\right)}$$

giving the strategy to derive an unknown rate constant (k2) at temperature (T2) by using a measured rate constant (k1) at temperature (T1).

Thus, kobs(pCH4, T) can be derived from kobs,t(pCH4, 298) fitted from double potential step chronoamperometry at 298 K (using polynomial regression (R2=0.99956) on Figure 6c to approach the real), and Ea,CH4 measured by UV-vis absorption spectroscopy (Figure 5f):

$$k_{obs}(p_{CH4}, T) = k_{obs},t\ (p_{CH4}, 298)e^{\frac{-E_{a,CH4}}{R}(\frac{1}{T}-\frac{1}{298})}$$

analogously, ksol(T) can be derived from ksol(298) and Ea,sol, which are extracted from the UV-vis absorption spectroscopy results:

$$k_{sol}(298) = k_{sol}(298)\ e^{\frac{-E_{a,sol}}{R}(\frac{1}{T}-\frac{1}{298})}$$

and the general form of FE(pCH4, T) is therefore given by the following equation:

$$FE(p_{CH4}, T) = \frac{k_{obs,t}\ (p_{CH4}\ ,298)\ e^{\frac{-E_{a,CH4}}{R}(\frac{1}{T}-\frac{1}{298})}}{k_{obs},\mathrm{t}\ (\mathrm{p}_{CH4},298)e^{\frac{-E_{a,CH4}}{R}(\frac{1}{T}-\frac{1}{298})}+k_{sol}298e^{\frac{-E_{a,sol}}{R}(\frac{1}{T}-\frac{1}{298})}}$$

See Figure 8 in main text and Table S13 for the estimated FE trend with respect to pCH4 and T.

3.3 Results and Discussion

Cyclic voltammograms under various p_{CH4} values in 98% H_2SO_4 support an electrocatalytic activation of CH_4 with Ag^I as the pre-catalyst. Experiments of cyclic voltammetry were conducted with 5 mM Ag_2SO_4 in 98% H_2SO_4 (c_{Ag} = 10 mM), under a single-chamber three-electrode setup at 258 ^oC (298 K) in a pre-defined pressure (Supporting Information, Figure S1), with fluorine-doped tin oxide (FTO) glass as an innocent working electrode.[2a, 9d] Figure 2a shows the lack of features in voltammogram (j-E relationship) without the addition of Ag_2SO_4 (yellow trace). In N_2 , voltammograms of Ag^I solution displayed an oxidative charge transfer peaking at $E_{p,a}$ = 1.82 V (all potentials are reported vs. Hg_2SO_4 /Hg electrode if not mentioned) before the onset of solvent oxidation at around 2.1 V (Figure 2 a and b).[17,19b] The corresponding

reduction peak of the electrochemically generated oxidant is observed predominantly at 1.08 V, albeit a minute peak dependent on scan rate (Figure 2b and c) and c_{Ag} (Figure S2) is visible at 1.52 V. The reductive peak at 1.08 V is assigned as a direct reduction of Ag^{II} into Ag^{I} . [19b] The secondary one at 1.52 V is suggested as the reduction of bisulfate radicals ($HSO_4^{\bullet}$) homogenously generated from the Ag-bound bisulfate ligand ($HSO_4^{\bullet}$) via a ligand-metal charge

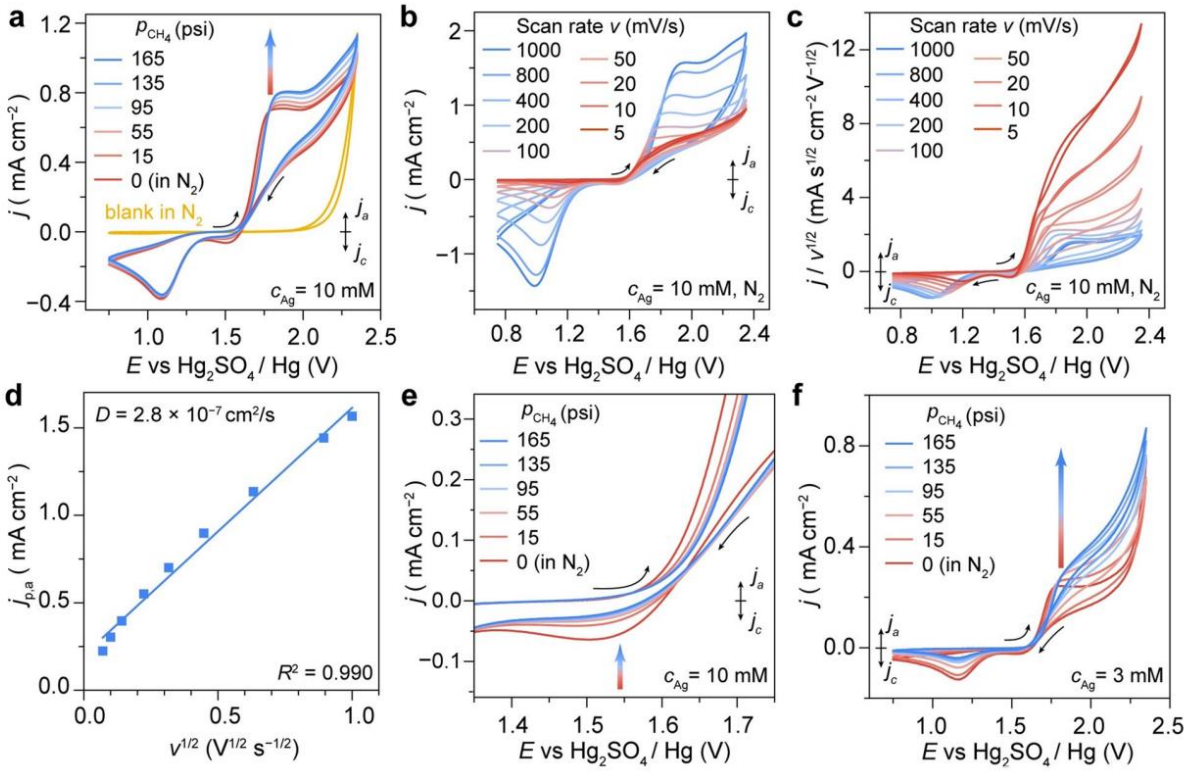

Figure 3.2: a) j-E plot when c_{Ag}=10 mM with increasing p_{CH4} (red to blue traces) and the result without Ag in N_2 (yellow trace, "blank in N_2"). b) j-E plot when c_{Ag}=10 mM in N_2 with various scan rates (v). c) $j/v^{1/2}$ –E plot from results shown in (b). d) The plot of anodic peak current density ($j_{p,a}$) versus $v^{1/2}$ from results shown in (b) and (c). D, the calculated diffusion coefficient. e) Enlarged j-E plot in (a) at around 1.5 V. f) j-E relationship when c_{Ag}=3 mM with increasing p_{CH4} . Unless noted, room temperature, 98% H_2SO_4 electrolyte, v=100 mVs^{-1} , and iR-compensated.

transfer (LMCT),[19b, 24] which helps explain why the integrated reductive charge is smaller than the oxidative one. We observed that the reaction kinetic responsible to the reductive peak at 1.52 V is sluggish since this peak is much less visible at a higher scan rate in Figure 2 b and c. Despite the noted complication of reductive behavior, the single-electron oxidation peak from Ag^{I} to Ag^{II} yields a satisfactory linear relationship in the Randles–Sevcik analysis[25] (Figure 2 c and d) with a diffusion coefficient of 2.8 X 10^{7} cm^{2} s^{-1} . Additional numerical simulation of cyclic voltammetry, whose details are listed in Figure S3, Table S1, and Table S2, not only supports the obtained value of diffusion coefficient but also suggests a quasi-reversible electrochemical oxidation of Ag^{I} as a desirable E step in an EC' mechanism with a charge-transfer rate constant (k_s) of 3 X 10^{-6} cm s^{-1} . When the N_2 environment was switched to CH_4 , a p_{CH4} -dependent change in the voltammograms was observed (Figure 2 a and S4). The current density of Ag^{I} oxidation increases with higher p_{CH4} values, along with the decrease of reductive current density peaking at 1.08 V. In addition, a noticeable disappearance of the reductive peak at 1.52 V was observed in CH_4 (Figure 2 e). As higher p_{CH4} values correlate with higher CH_4 concentrations in the electrolyte, the observed change in voltammograms is consistent with a hypothesized EC' mechanism mediated by electrogenerated Ag^{II} (Figure 1 c), in which the increased oxidative current density stems from the regenerated Ag^{I} near the electrode after an oxidative CH_4 activation. The disappearance of reductive peak at 1.52 V in CH_4 suggests that CH_4 competitively reacts with Ag^{II} metalloradical in lieu of LMCT on the $HSO_4^{\bullet}$ ligand, hinting the presence of a radical-based reaction pathway. We note that at room temperature CH_4 only possesses a solubility of about 0.8 mM at ambient pressure and less than 9 mM at the highest tested pressure (p_{CH4} = 165 psi, see the Supporting Information), a concentration smaller than the

c_{Ag} used in Figure 2 a to e (c_{Ag} = 10 mM). This suggests mass transport of CH_4 may limit the catalytic response shown in Figure 2 a. Evidently, when c_{Ag} = 3 mM, j-E relationship displays a more pronounced catalytic current of CH_4 activation, even at ambient pressure (15 psi) (Figure 2 f). This confirms that the electrocatalytic behavior in cyclic voltammetry is limited by the solubility of CH_4 and electrogenerated Ag^{II} is ambiently reactive towards CH_4 .

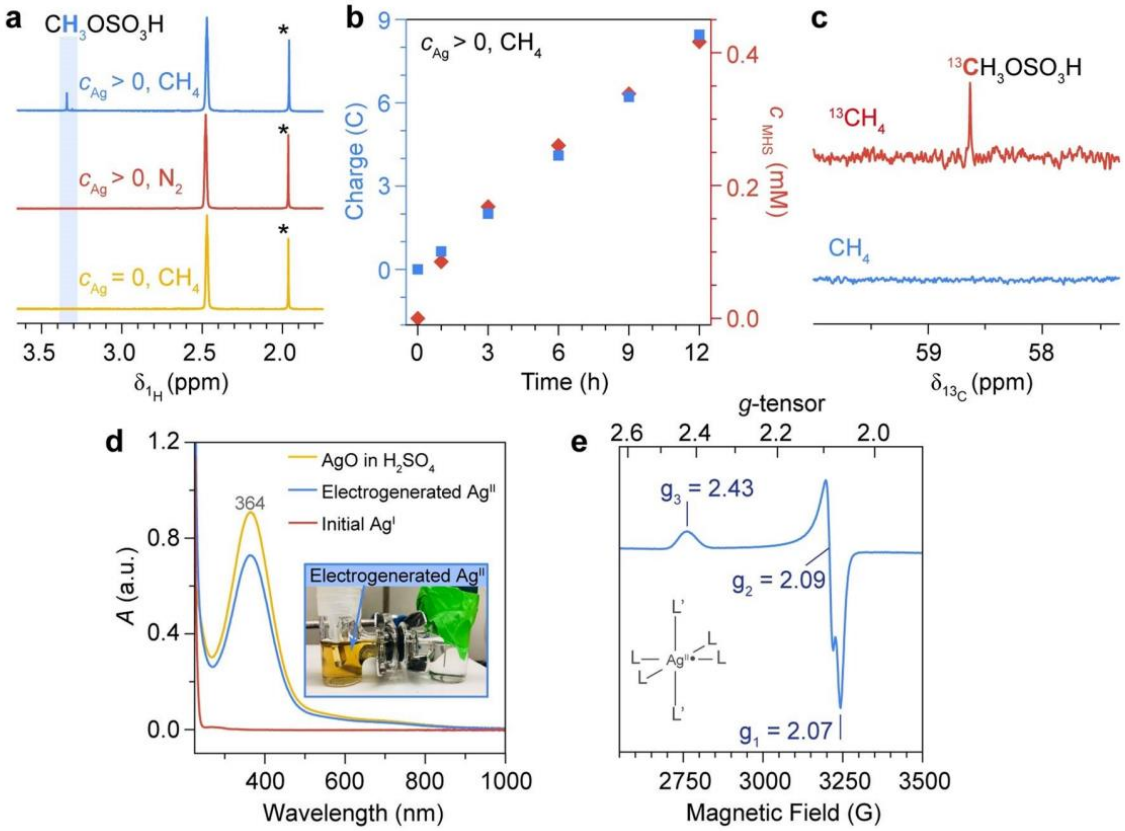

Figure 3.3: a) ^{1}H-NMR spectra of solutions after a 3-h electrolysis with c_{Ag}=10 mM in CH_4 (blue) and N_2 (red) or c_{Ag}= 0 mM in CH_4 (yellow). E=1.637 V; *, Acetic acid as internal standard; [D_6]DMSO. b) The evolution of electric charges (blue) and CH_3OSO_3H concentration (c_{MHS}, red) during a 12-h electrolysis. 25 ^{o}C; c_{Ag}= 10 mM; E = 1.602 V. c) ^{13}C-NMR spectra of solutions after a 3-h electrolysis with c_{Ag} = 3 mM in $^{13}CH_4$ (red) and CH_4 of natural abundance (blue). [D_6]DMSO; E = 1.637 V. d) UV/Vis spectra of the pre-catalyst Ag^{I} (red),

electrogenerated Ag^{II} (blue), and AgO dissolved in 98% H_2SO_4 (yellow). The inset shows the yellow colored electrogenerated Ag^{II}. e) EPR spectrum of AgO in 98% H_2SO_4 (77 K).

The proposed electrocatalytic CH_4 activation is corroborated by analyzing the solution after electrolysis via ^1H nuclear magnetic resonance (^1H-NMR) spectroscopy. Room-temperature preparative bulk electrolysis (t = 3 h) was conducted at c_{Ag} = 10 mM in a two-chamber three-electrode setup (Figure S5), and the composition of the resultant electrolyte in the anodic chamber was analyzed by ^1H-NMR spectroscopy. Electrolysis at E = 1.637 V and p_{CH4} = 15 psi (ambient pressure) leads to the emergence of a peak at chemical shift d = 3.34 ppm in ^1H-NMR spectra (blue trace in Figure 3 a), consistent with a presumed formation of CH_3OSO_3H (Figure S6a). CH_3OSO_3H formation was not observed either in N_2 with Ag^I or in CH_4 devoid of Ag^I (red and yellow trace in Figure 3 a, respectively). The amount of generated CH_3OSO_3H is proportional to the amount of electric charge passed and linear to t up to 12 h when E = 1.602 V (Figure 3 b). This suggests that the CH_3OSO_3H production is persistent in CH_4 . Attempts of detecting gas phase products with an online gas chromatograph (Figure S1a) did not find any detectable CO, CO_2 , and other carbon-based products (Figure S7). ^{13}C isotope-labeling experiment with $^{13}CH_4$ in electrolysis led to a signal at d = 58.6 ppm in ^{13}C-NMR spectrum hence $^{13}CH_3OSO_3H$ formation, which was not observable under CH_4 of natural isotope abundance (Figure 3 c). Those data support an electrocatalytic functionalization of CH_4 into CH_3OSO_3H with minimal carbon-based side products.

Additional experimental data support a CH_4 -activating electrocatalysis mediated by Ag^{II}. Visual inspection during electrolysis unveiled a yellow hue in solution near the FTO electrode under potentials anodic enough to produce Ag^{II} (insets in Figure 3 d and S2), which faded away after

the termination of electrochemical oxidation. UV/Vis spectroscopy recorded an absorption peak at 364 nm with a shoulder around 700 nm (blue trace in Figure 3 d) that existed for more than 10 min after electrolysis (Figure S8a). Such absorption features are distinct from the stable spectrum of Ag^{I} (red trace in Figure 3 d) and identical to the one of commercially available AgO dissolved in 98% H_2SO_4 (yellow trace in Figure 3 d and more in Figure S8b). In the solution of AgO, a distorted octahedral Ag^{II} metalloradical depicted in Figure 1 c is confirmed via electron paramagnetic resonance (EPR) spectroscopy[19b, 26] with our measured spectrum at 77 K (Figure 3 e; $g_1 = 2.07$, $g_2 = 2.09$, $g_3 = 2.43$). Given the similar optical spectra, we deemed that Ag^{II} metalloradical is generated upon electrochemical oxidation. Moreover, we found that the solution of AgO is reactive towards CH_4 ambiently and yields CH_3OSO_3H, albeit with weaker reactivity (Figure S6b). This observation supports our initial inspiration that Ag^{II} as a soft Lewis acid is reactive towards CH_4 and corroborates our proposed EC' mechanism mediated by Ag^{II} (Figure 1 c). Last, when oleum (20% free SO_3 basis) was employed as the electrolyte, the predominant product was methanesulfonic acid (CH_3SO_3H) with a minute amount of CH_3OSO_3H (31:1 ratio) (Figure S6c). The detection of CH_3SO_3H from oleum suggests that electrolysis generates SO_3 -reactive CH_3 C, [7a] consistent with the implication from HSAB theory due to $CH_3^{\bullet}$'s softness (Figure 1 a).

We evaluated the reactivity of CH_4 activation as a function of electrochemical potential E, CH_4 pressure p_{CH4} , and electrolysis duration t. When $c_{Ag} = 0.5$ mM and $p_{CH4} = 15$ psi, the partial current density (j_{CH4}) and the Faradaic efficiency (FE) of CH_3OSO_3H formation, quantified by ^{1}H-NMR (Figure S6d, Table S3), are displayed against E in Figure 4 a. CH_3OSO_3H formation takes place when E > 1.5 V, concurrent with Ag^{II} generation in Figure 2 b. A near-plateaued j_{CH4} at higher E contributes to a maximal FE of 36.2% at 1.662 V when $c_{Ag} = 0.5$ mM (Figure 4 a).

This observed optimum of electrocatalytic CH_4 functionalization is about 600 mV more cathodic than our previously reported vanadium-oxo electrocatalyst[2a] and comparable with the Pd-based ones in literature. [9] As the observed j_{CH4} plateau does not change significantly when c_{Ag} = 10

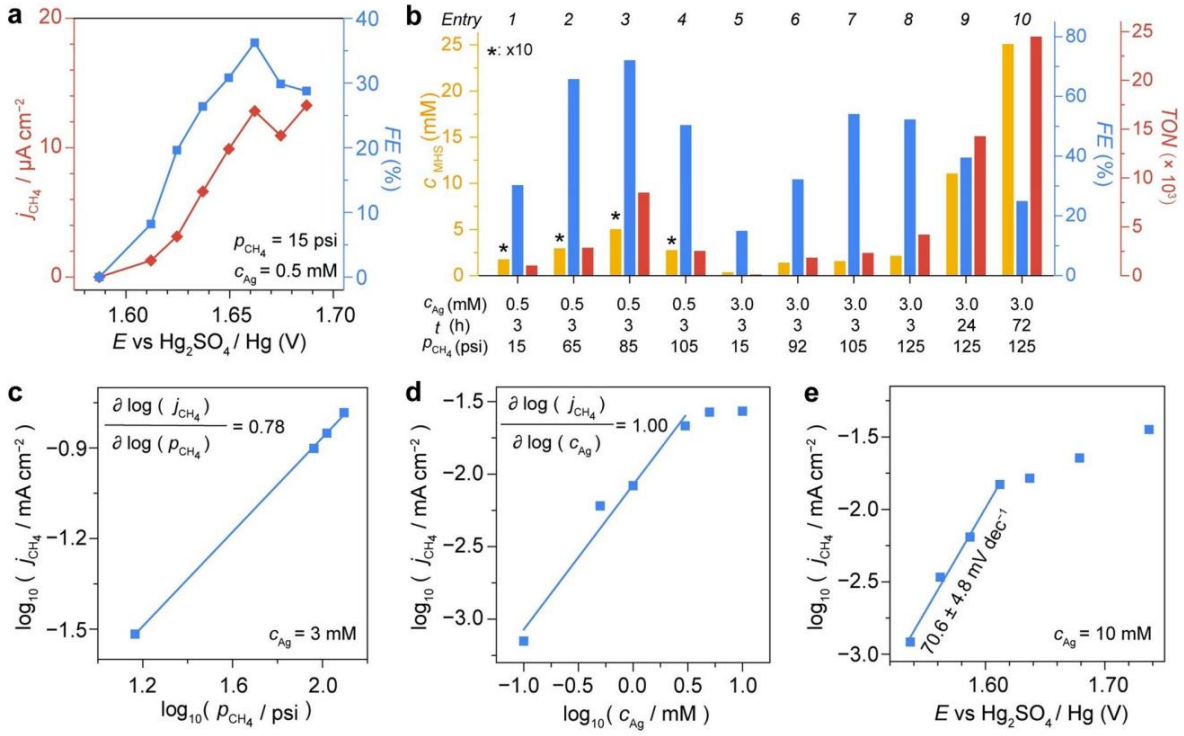

Figure 3.4: a) Partial current density (j_{CH4} , red) and Faradaic efficiencies (FE, blue) as a function of E. t = 3 h. b) Concentration of accumulated CH_3OSO_3H (c_{MHS}, yellow), FE (blue), and turnover numbers (TONs, red) at different values of p_{CH4} , t, and c_{Ag}. E = 1.737 V; *, Multiplied by a factor of 10. c) The plot of $\log_{10}(j_{CH4})$ versus $\log_{10}(p_{CH4})$. E=1.737 V. d) The plot of $\log_{10}(j_{CH4})$ versus $\log_{10}(c_{Ag})$. p_{CH4} =15 psi; E = 1.637 V. e) The plot of $\log_{10}(j_{CH4})$ versus E. p_{CH4} = 15 psi. Each data point is the average of at least two or three independent measurements. 25 °C.

mM (Figure S9, Table S3), it is the mass transport of CH_4 that limits both the j_{CH4} and FE since Ag^{II} seems highly reactive towards CH_4 and CH_4's solubility is about 0.8 mM ambiently (see the Supporting Information).[27] Additional evaluation was conducted under elevated pressures when c_{Ag} = 0.5 (entry 1 to 4) and 3 mM (entry 5 to 10) in Figure 4 b. When t = 3 h (entry 1 to 8 in Figure 4 b), increasing p_{CH4} leads to increased FE and j_{CH4} and results in a maximal FE of 72.1% at c_{Ag} = 0.5 mM, p_{CH4} = 85 psi, and E = 1.737 V (Table S4). When p_{CH4} = 15 and 85 psi, our reported data suggest a full-cell voltage of 1.07 and 1.15 V, respectively, for an electricity-driven CH_4 functionalization with the reduction O_2 into H_2O as the reduction half-reaction, in comparison to the thermodynamic driving force of 0.48 V and 0.50 V based on our calculation (Table S5). The ideal energy input, assuming a unity of FE, is 210 and 220 kJ mol_{CH4}^{-1} (Table S6) when p_{CH4} = 15 and 85 psi, respectively, in the context of a lower heating value (LHV) of 802 kJ mol_{CH4}^{-1} for CH_4 . Comparing the results when c_{Ag} = 0.5 (entry 1 to 4) and 3 mM (entry 5 to 10) in Figure 4 b, higher c_{Ag} values increase CH_3OSO_3H concentration (c_{MHS}) yet lower FE values, likely due to the CH_4's limited solubility. Extending t from 3 h to 72 h yielded c_{MHS} > 25 mM when c_{Ag} = 3 mM (25 ^oC, p_{CH4} = 125 psi, and E = 1.737 V; entry 9 and 10 in Figure 4 b, S10, and Table S7). While there remains much room for optimization, the reported values of FE and c_{MHS} illustrate the favorable intrinsic activity and practical usability of this ambient electrocatalytic CH_4 activation.

Electrocatalytic kinetics was determined to be first-order on both CH_4 and Ag^{II} with a turnover-limiting CH_4 activation and a high value of pseudo-first-order rate constant k_{obs}. Devoid of mass-transport complication, j_{CH4} as a surrogate of the CH_4 -activation rate is found to be mostly linear with $p_{CH}4$. When c_{Ag} = 3 mM and E = 1.737 V, $\partial\log_{10}(j_{CH4})/\partial\log_{10}(p_{CH4})$ = 0.78 (Figure 4 c, Table S4). Experiments with c_{Ag} as a proxy of electrogenerated Ag^{II} yielded $\partial\log_{10}(j_{CH4}$

)/$\partial\log_{10}(c_{Ag})$ = 1.00 when p_{CH4} = 15 psi and E = 1.637 V (Figure 4 d, Table S8). Those results suggest that the turnover-limiting step probably involves one equivalent of CH_4 and Ag^{II}. Plotting $\log_{10}(j_{CH4})$ versus E when c_{Ag} = 10 mM and p_{CH4} = 15 psi yielded a Tafel slope of 70.6 : 4.8 $mVdec^{-1}$ (Figure 4 e, Table S3). The obtained value of Tafel slope is in accordance with a proposed EC' mechanism with a continuous regeneration of Ag^{II} (E step) and a turnover-limiting CH_4 -activating C' step (Figure 1 c), which predicts a theoretical value of 60 mV/dec for Tafel slope. [28] The obtained reaction kinetics on Ag enables us to calculate $k_{obs,b}$ as the pseudo-first-order rate constant of CH_4 activation,[29] frequently dubbed as turnover frequency, based on bulk electrolysis data (hence the subscript "b").[2a, 30] At 25 ^oC, c_{Ag} = 0.5 mM, and E = 1.737 V, $k_{obs,b}$ reaches as high as 3.5 X 10^2 and 2.8 X 10^3 h^{-1} when p_{CH4} = 15 and 85 psi, respectively (Table S4). The values of $k_{obs,b}$ are on par with some of the best electrocatalysts for CH_4 activation (Table S9).[2a, 9d, 11c] Furthermore, we calculated the effective turnover number (TON) of CH_4 activation, presented in Figure 4 b. [30a,b] Similarly due to CH_4's limited solubility (see above), higher c_{Ag} yielded lower TON when comparing between c_{Ag} = 0.5 (entry 1 to 4) and 3 mM (entry 5 to 10) in Figure 4 b. Prolonged electrolysis increases the calculated TON values. When t = 72 h and p_{CH4} = 125 psi, TON tops 2.45 X 10^4 (entry 10 in Figure 4 b, Table S7) and no intrinsic issue seems to prevent the electrocatalytic system from keeping operation. The obtained TON value showcases the longevity of the discovered electrocatalyst.

We found that CH_4 activation is kinetically favored over the undesirable side reaction of solvent oxidation. In 98% H_2SO_4 electrogenerated Ag^{II} either activates CH_4 or reacts with solvent possibly via a $HSO_4^{\bullet}$ -yielding LMCT (see above). We quantitatively established a reaction model that includes two competing reaction pathways: CH_4 activation and the undesirable solvent oxidation (Figure 5 a). The $k_{obs,b}$ calculated from bulk electrolysis offers the first

approach for elucidating the kinetics of CH_4 activation branch ("method 1" in Figure 5 a). We also took advantages of the difference in optical absorption between Ag^I and Ag^{II} (Figure 3 d and S2) and the equivalent identity of Ag^{II} in the AgO solution and the post-electrolyzed Ag^I solution (Figure S8, see above), and henceforth employed the Ag^{II}'s absorbance at 364 nm (A_{364}) of AgO

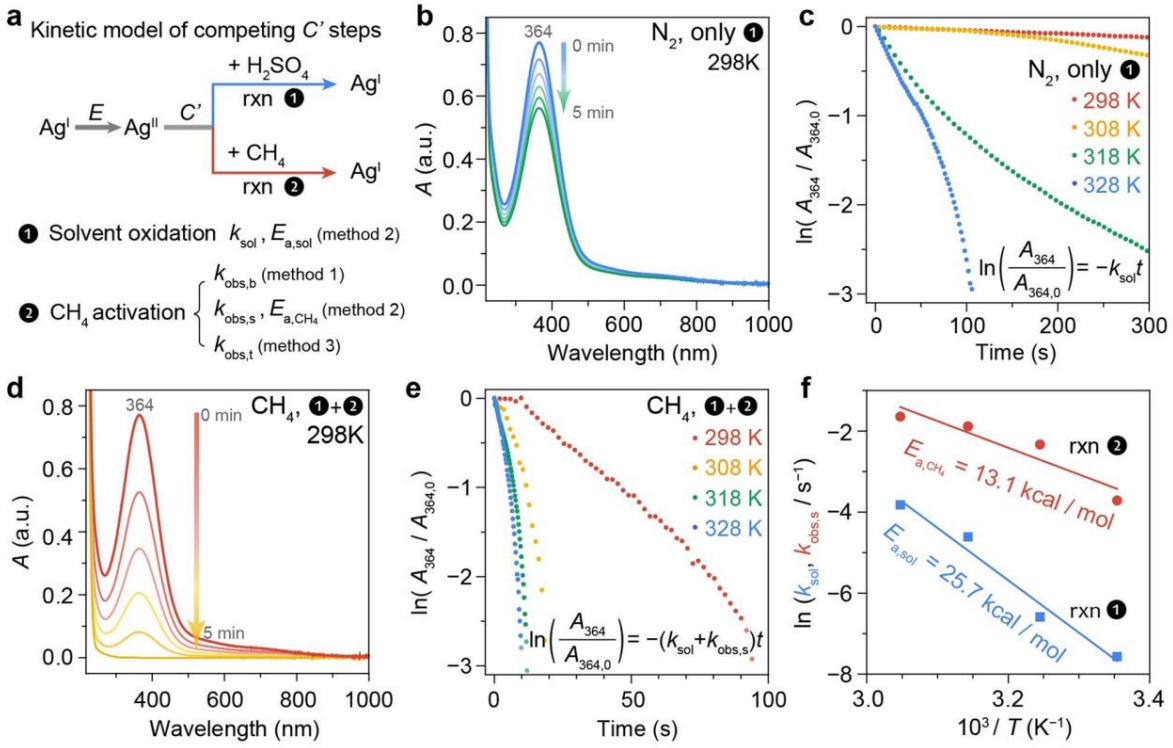

Figure 3.5: a) A kinetic model that includes competing Ag^{II}-based solvent oxidation (**1**) and CH_4 activation (**2**), which were studied via steady-state bulk electrolysis ("method 1"), temperature-dependent UV/Vis absorption spectroscopy ("method 2"), and double potential step chronoamperometry ("method 3"). (b to e) The time evolutions of Ag^{II}'s absorption spectra at 298 K (b, d) and the logarithmic of normalized absorbance at 364 nm $\ln(A_{364}/A_{364,0})$ under different temperatures (c, e) when p_{CH4} = 0 (b, c) and 15 psi (d, e). f) The logarithmic of pseudo-first-order rate constant for solvent oxidation ($\ln(k_{sol})$, blue) and CH_4 activation ($\ln(k_{obs,s})$, red)

versus the inverse of temperature (1/T). $E_{a,sol}$ and $E_{a,CH4}$, the calculated activation energies for Ag^{II}-based solvent oxidation and CH_4 activation, respectively.

solution to probe the transient of Ag^{II} at different temperatures ("method 2" in Figure 5 a, see the Supporting Information). When p_{CH4} = 0 psi, the initial decrease of A_{364} from Ag^{II} followed a

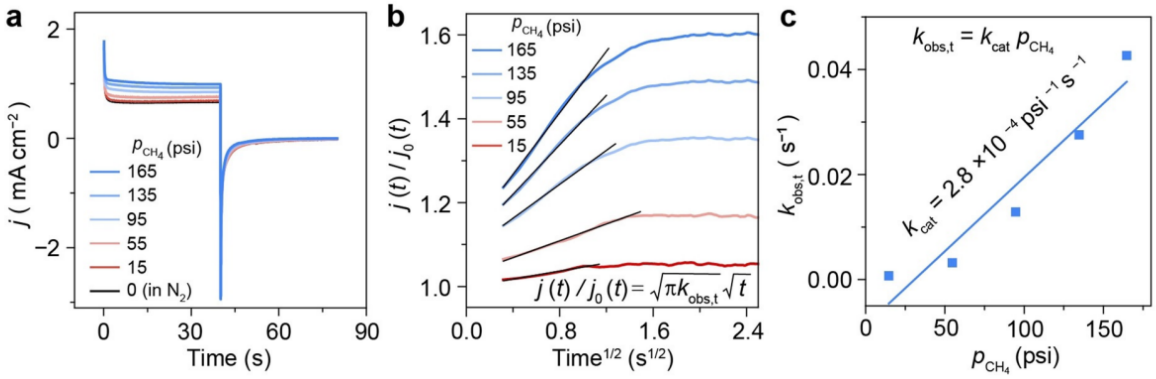

Figure 3.6: a) Double potential step chronoamperometry at different p_{CH4} . E = 2.0 and 0.75 V for time t ∈ [0, 40 s] and t ∈ [40 s, 80 s], respectively; c_{Ag} = 10 mM. b) The plot of $j(t)/j_0(t)$ versus $t^{1/2}$ based on the results in (a) at different p_{CH4} . j_0 (t) and j(t), current densities at time t when p_{CH4} = 0 and $p_{CH4} \neq 0$, respectively. c) Pseudo-first-order rate constant $k_{obs,t}$ for CH_4 activation extracted from the linear region in (b) as a function of p_{CH4} .

first-order kinetics for solvent oxidation (Figure 5 b and c), which possesses a rate constant k_{sol} = 1.9 h^{-1} at 25 °C and an activation energy $E_{a,sol}$ = 25.7 kcal mol^{-1} (Figure 5 f, Table S10). When p_{CH4} = 15 psi, the initial A_{364} decrease contributed from both solvent oxidation and CH_4 activation similarly followed a first-order kinetics and was much faster (Figure 5 d and e). The resultant pseudo-first-order rate constant of CH_4 activation from absorption spectroscopy (hence

the subscript "s") $k_{obs,s}$ = 88 h^{-1} at 25 °C with an activation energy $E_{a,CH4}$ = 13.1 kcal mol^{-1} (Figure 5 f, Table S10). Furthermore, although our setup of UV/Vis absorption spectroscopy is unable to operate at elevated pressure, experiments of double potential step chronoamperometry[28] at higher values of p_{CH4} indicate that k_{obs} is linearly dependent on p_{CH4} ("method 3" in Figure 5 a). At a certain p_{CH4} value, E was first poised at 2.0 V to oxidatively generate Ag^{II} population near the electrode; then E was switched to 0.75 V at which potential the residual Ag^{II} that had not reacted was reduced back to Ag^{I} . Right after the potential application of 2.0 V on the electrode, current density j was recorded under different p_{CH4} (Figure 6 a). Qualitatively, the higher steady-state j(t) under higher p_{CH4} at 2.0 V indicates a CH_4 -mediated electrocatalysis while the constant steady state j(t) at 0.75 V suggests that a Ag-based catalytic cycle imposes no loss of Ag in the solution. If $j_0(t)$ is denoted as the transient j(t) value when p_{CH4} = 0 psi, $k_{obs,t}$ based on such transient measurement (hence the subscript "t") can be mathematically described:

$$\frac{j(t)}{j_0(t)} = \sqrt{\pi k_{obs,t}}\sqrt{t}$$

The plots of $j(t)/j_0(t)$ versus $t^{1/2}$ at various p_{CH4} values are displayed in Figure 6 b and the calculated $k_{obs,t}$ values are mostly linear to p_{CH4} (Figure 6 c, Table S11). The slope of $k_{obs,t}$ versus p_{CH4} , at a value of 2.8 X 10^{-4} psi^{-1} s^{-1} , yields k_{cat} as the second-order rate constant of the bimolecular reaction between Ag^{II} and CH_4 . The observed linear relationship between $k_{obs,t}$ and p_{CH4} offers another evidence that the Ag^{II} - based CH_4 activation is the turnover-limiting step. Overall, the rate constants of Ag^{II}-based CH_4 activation were determined via three independent methods (Figure 5 a): steady state bulk electrolysis ($k_{obs,b}$), time-dependent absorption spectroscopy ($k_{obs,s}$), and double potential step chronoamperometry ($k_{obs,t}$). Notwithstanding the

values of $k_{obs,s}$ fetched when c_{Ag} > 10 mM, a satisfactory agreement was reached at low c_{Ag} value (Table S12). The larger rate constant and the lower value of activation energy for CH_4 activation suggest that during ambient electrocatalysis CH_4 functionalization is order-of-magnitude faster than the undesirable solvent oxidation

Our results warrant a mechanistic discussion in this electrocatalytic CH_4 activation inspired by HSAB theory (Figure 7). We showed that an electrochemical oxidation of Ag^{I} yields Ag^{II} metalloradical continuously (E step and route i in Figure 7). EPR spectroscopy supports Ag^{II}'s radical nature and the quasi-reversible oxidative charge transfer is supported by the successful application of Randles–Sevcik analysis and numerical simulation.[25] Without CH_4 , Ag^{II} slowly undergoes solvent oxidation (route ii in Figure 7; k_{sol} = 1.9 h^{-1} and $E_{a,sol}$ = 25.7 kcal mol^{-1} at 25 ^{o}C), possibly via a $HSO4^{\bullet}$ -yielding LMCT[19b, 31] as evident in the reductive peak of 1.52 V in the cyclic voltammogram. The resultant $HSO4^{\bullet}$ is proposed to further dimerize and yield persulfate, which eventually can disproportionate and generate O_2 (Figure S11).[19b, 32] In CH_4 , a turnover-limiting reaction between one equivalent of Ag^{II} and CH_4 initiates CH_4 activation (route iii in Figure 7). The first-order reaction kinetics for both Ag^{II} and CH_4 has been supported by the near-unity values of $\partial\log_{10}(j_{CH4})/\partial\log_{10}(p_{CH4})$ and $\partial\log_{10}(j_{CH4})/\partial\log_{10}(c_{Ag})$ in bulk electrolysis, the time-dependent change of A_{364} for Ag^{II}, and the experiments of double potential step chronoamperometry. The reported pseudo-first-order rate constant k_{obs} = 3.5 X 10^2 or 88 h^{-1} ($k_{obs,b}$ and $k_{obs,s}$, respectively) at 25 ^{o}C and p_{CH4} = 15 psi with $E_{a,CH4}$ = 13.1 kcal mol^{-1} . The quantitative determination of reaction kinetics offers opportunities for additional understanding and design of the reported electrocatalytic system.

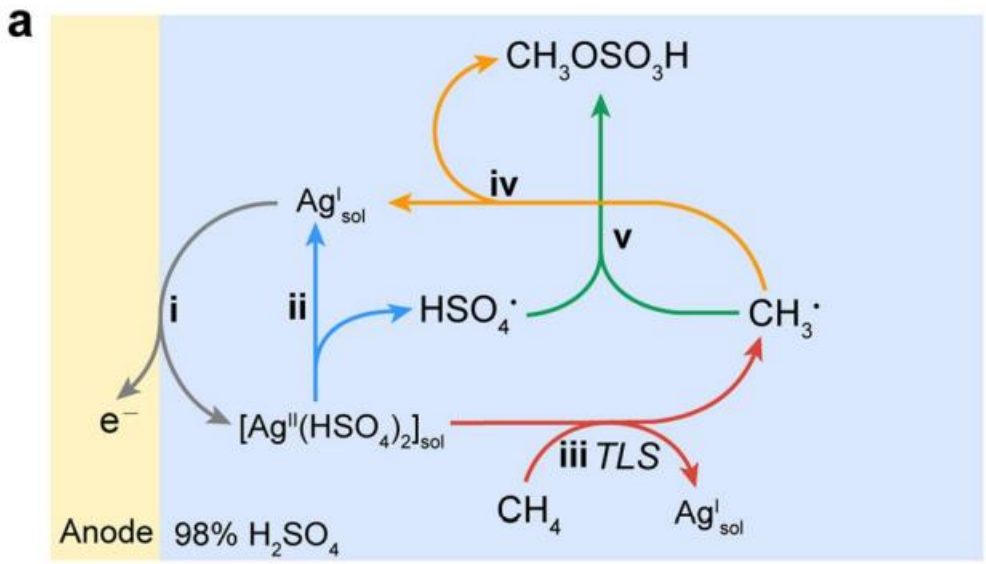

b

***E* step:** Electrochemical generation of Ag^{II}

i $Ag^I_{sol} + 4/3\ H_2SO_4 + 2/3\ HSO_4^- \longrightarrow [Ag^{II}(HSO_4)_2]_{sol} + 4/3\ H^+ + e^-$

Side reaction: Solvent oxidation

ii $[Ag^{II}(HSO_4)_2]_{sol} \longrightarrow Ag^I_{sol} + HSO_4^{\cdot} + HSO_4^-$

$E_{a,sol}$ = 25.7 kcal/mol

***C'* step:** CH_4 functionalization

iii *TLS* $[Ag^{II}(HSO_4)_2]_{sol} + CH_4 \longrightarrow Ag^I_{sol} + CH_3^{\cdot} + H_2SO_4 + HSO_4^-$

iv $[Ag^{II}(HSO_4)_2]_{sol} + CH_3^{\cdot} \longrightarrow Ag^I_{sol} + CH_3OSO_3H + HSO_4^-$

v $HSO_4^{\cdot} + CH_3^{\cdot} \longrightarrow CH_3OSO_3H$

C' step (iii + iv)

$2\ [Ag^{II}(HSO_4)_2]_{sol} + CH_4 \longrightarrow 2\ Ag^I_{sol} + CH_3OSO_3H + H_2SO_4 + 2\ HSO_4^-$

E_{a,CH_4} = 13.1 kcal/mol

Overall electrocatalytic oxidation: i × 2 + (iii + iv)

$$CH_4 + H_2SO_4 \xrightarrow[98\ \%\ H_2SO_4]{Ag\ cat.,\ 25\ ^\circ C} CH_3OSO_3H + 2\ H^+ + 2\ e^-$$

Figure 3.7: a) A proposed catalytic cycle. b) Individual steps i to v in the catalysis and the overall electrocatalytic oxidation reaction. TLS = turnover-limiting step

We pondered whether Ag^{II} is directly responsible to turnover-limiting C—H activation in CH_4 (C' step and route iii in Figure 7) and the nature of reactions after CH_4 activation during catalysis (route iv and v in Figure 7). We contend that $HSO4^{\bullet}$ generated from the LMCT of Ag-bound $HSO4^{-}$ has a minimal contribution, if any, in the turnover-limiting step of Ag^{II}-initiated CH_4 activation, not only because the inclusion of $HSO4^{\bullet}$ will prevent a first-order kinetics for both Ag^{II} and CH_4 but also because $HSO4^{\bullet}$ thermally generated from persulfate is reported as inactive towards CH_4 . [2a, 9b] The electrolysis in oleum with yielded CH_3SO_3H suggests the presence of $CH_3^{\bullet}$ intermediate. [7a] As η = 6.7, 6.42, and 4.87 for Ag^{II}, $H^{\bullet}$, and $CH_3^{\bullet}$, respectively, [5] we postulate a homolytic CH_4 cleavage in the turnover-limiting step, while we do not exclude the possibility of a Ag-CH_3 intermediate from electrophilic activation. The reaction steps after the turnover-limiting step of CH_4 activation remain elusive. We tentatively consider that the yielded $CH_3^{\bullet}$ can either directly react with another Ag^{II} for a consecutive two-electron oxidation (route iv in Figure 7), or react with one $HSO4^{\bullet}$ indirectly generated from Ag^{II} to yield CH_3OSO_3H (route v in Figure 7). Nonetheless, as shown by our data, the branch of CH_4 -activating pathway is kinetically faster than the solvent oxidation at room temperature and ambient pressure, paving a selective electrocatalytic CH_4 activation. Assuming two consecutive Ag^{II}-mediated oxidations for one equivalent of CH_4 activation (route iii and iv in Figure 7), the half-reaction of overall electrocatalysis is written as:

$$CH_{4\,(g)} + H_2SO_{4\,(l)} \rightarrow CH_3OSO_3H_{\,(l)} \rightarrow 2H^{+}\,(\text{solvated}) + 2e^{-} \qquad (2)$$

Last, the quantification of reaction kinetics indulges us to predict the electrocatalysis's ultimate performance when all of the engineering constraints, particularly the mass transport of CH_4 , are successfully addressed in a hypothetical scenario. In particular, we are interested in the FE

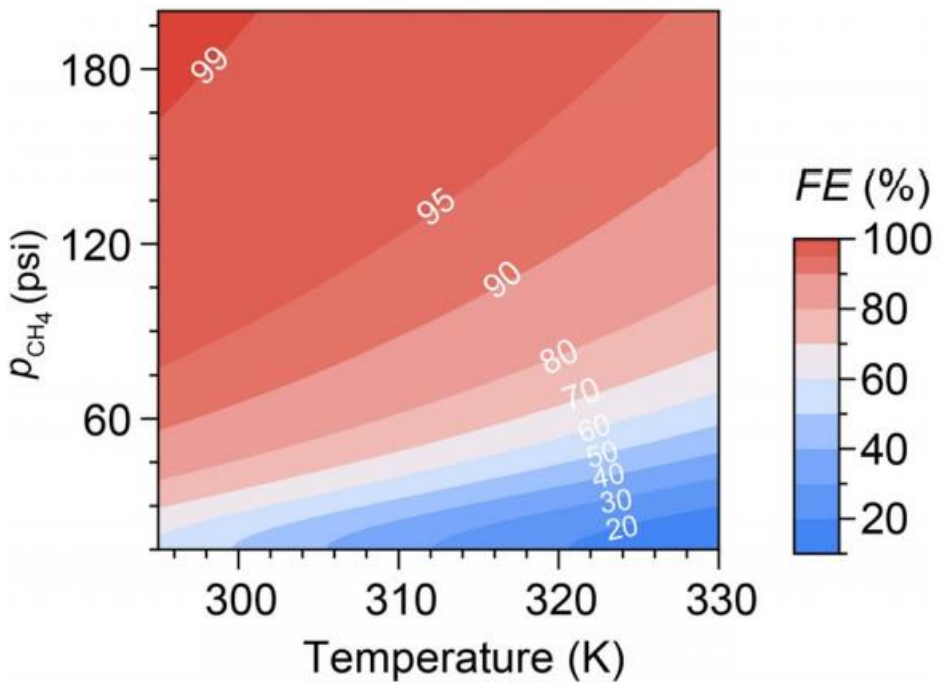

Figure 3.8: Calculated FE as a function of p_{CH4} and T based on the established kinetic model and the measured kinetic parameters.

towards CH_4 functionalization. Our established kinetic model (Figure 5 and 6) suggests that the pseudo-first-order kinetic rate constant of CH_4 activation and the selectivity towards CH_4 activation are both functions of CH_4 pressure p_{CH4} and temperature T, that is, $k_{obs} = k_{obs}(p_{CH4}, T)$ and $FE = FE(p_{CH4}, T)$. We utilized our kinetic model shown in Figure 5 a and calculated the values of FE (p_{CH4} , T) as a function of p_{CH4} and T (Figure 8, Table S13):

$$FE\ (p_{CH4}, T) = \frac{k_{obs,t}\ (p_{CH4}, 298)\ e^{\frac{-E_{a,CH4}}{R}(\frac{1}{T}-\frac{1}{298})}}{k_{obs,t}\ (p_{CH4}, 298) e^{\frac{-E_{a,CH4}}{R}(\frac{1}{T}-\frac{1}{298})} + k_{sol} 298 e^{\frac{-E_{a,sol}}{R}(\frac{1}{T}-\frac{1}{298})}}$$

At T= 25 ^{o}C (298 K), FE(p_{CH4} , T) is calculated as 53% at ambient pressure (p_{CH4} = 15 psi). FE reaches 90% when p_{CH4} > 62 psi (4.3 bar), 95% when p_{CH4} > 85 psi (5.9 bar), and 99% when p_{CH4} > 180 psi (12.4 bar) (Figure 8). This suggests that Ag-based electrocatalysis of CH_4 activation is capable of reaching near-unity selectivity at room temperature and an accessible p_{CH4} that is much lower than the syngas synthesis from steam reforming of CH_4 (650 ^{o}C and 30 bar).[33] We also considered how reaction temperature T affects FE (Figure 8). FE drops significantly at higher temperature, because $E_{a,sol} > E_{a,CH4}$ and hence the rate of solvent oxidation increases much faster than the one of CH_4 activation. This suggests that Ag^{II}-mediated electrocatalysis is selective and specifically suitable at lower temperature. While the absolute rate of CH_4 activation increases with temperature, it is the competition between CH_4 activation and the undesirable solvent oxidation that dictates the selectivity. Overall, calculations of FE (p_{CH4} , T) suggest that the Ag^{II} - mediated electrocatalysis is reactive and selective for low-temperature CH_4 functionalization and further engineering optimization will be constructive to reach the electrocatalyst's full potential.

3.4 Conclusion

Inspired by the HSAB theory, we explored the electrocatalytic CH_4 functionalization mediated by Ag^{II} metalloradical, the last class (b) metal whose reactivity towards CH_4 is unknown. Kinetic characterization establishes that selective electrocatalytic CH_4 activation proceeds ambiently in 98% H_2SO_4 with low activation energy and high kinetic rate constant. The electrocatalytic system is unique that low reaction temperature is preferred for high reaction selectivity, while a reaction pressure slightly higher than ambience (6 – 10 bar) favors the overall turnover. Future experiments are desired to continue investigating the nature of reactions after the turnover-limiting CH_4 activation. Engineering optimization is needed to overcome the mass transport

limitation due to CH_4 limited solubility and maximize the electrocatalysis's selectivity at low temperature. Moreover, the successful inquiry of CH_4 catalysts initiated based on the chemical hardness of possible reaction intermediates encourages us to adopt such a strategy to discover more CH_4 -activating catalysts, particularly with electrochemical charge transfer as the reaction's driving force. This work offers a new route of ambient electrocatalytic CH_4 functionalization as well as a strategy that may be generally applicable for future catalyst design, in order to achieve chemical production from widely distributed natural gas resources with minimal infrastructure reliance.

Data availability: All data reported or included in this analyzed during this study are included in this published article (and its supplementary information).

3.5 References

1. a) D. Malakoff, Science 2014, 344, 1464 – 1467; b) O. Edenhofer, R. Pichs-Madruga, Y. Sokona, J. C. Minx, E. Farahani, K. Susanne, K. Seyboth, A. Adler, I. Baum, S. Brunner, P. Eickemeier, B. Kriemann, J. Savolainen, S. Schlomer, C. von Stechow, T. Zwickel, Working Group III, Contribution to the Fifth Assessment Report of the Intergovernmental Panel on Climate Change, Climate Change 2014: Mitigation of Climate Change, Cambridge University Press, 2015; c) J. F. Hartwig, J. Am. Chem. Soc. 2016, 138, 2 – 24.

2. a) J. Deng, S.-C. Lin, J. Fuller, J. A. IÇiguez, D. Xiang, D. Yang, G. Chan, H. M. Chen, A. N. Alexandrova, C. Liu, Nat. Commun. 2020, 11, 3686; b) N. J. Gunsalus, A. Koppaka, S. H. Park, S. M. Bischof, B. G. Hashiguchi, R. A. Periana, Chem. Rev. 2017, 117, 8521 – 8573; c) X. Meng, X. Cui, N. P. Rajan, L. Yu, D. Deng, X. Bao, Chem 2019, 5, 2296 – 2325.

3. R. G. Parr, R. G. Pearson, J. Am. Chem. Soc. 1983, 105, 7512 – 7516.

4. R. G. Parr, L. v. Szentp#ly, S. Liu, J. Am. Chem. Soc. 1999, 121, 1922 – 1924.

5. R. G. Pearson, Inorg. Chem. 1988, 27, 734 – 740.

6. a) R. A. Periana, D. J. Taube, H. Taube, E. R. Evitt (Catalytica, Inc.), U.S. Patent 5,306,855, 1994; b) R. A. Periana, D. J. Taube, E. R. Evitt, D. G. Löffler, P. R. Wentrcek, G. Voss, T. Masuda, Science 1993, 259, 340 – 343; c) B. G. Hashiguchi, M. M. Konnick, S. M. Bischof, S. J. Gustafson, D. Devarajan, N. Gunsalus, D. H. Ess, R. A. Periana, Science 2014, 343, 1232 – 1237.

7. a) N. Basickes, T. E. Hogan, A. Sen, J. Am. Chem. Soc. 1996, 118, 13111 – 13112; b) A. E. Sherry, B. B. Wayland, J. Am. Chem. Soc. 1990, 112, 1259 – 1261.

8. a) X. X. Zhang, B. B. Wayland, J. Am. Chem. Soc. 1994, 116, 7897 – 7898; b) M. Lin, A. Sen, Nature 1994, 368, 613 – 615.

9. a) R. A. Periana, O. Mironov, D. Taube, G. Bhalla, C. J. Jones, Science 2003, 301, 814 – 818; b) R. S. Kim, A. Nazemi, T. R. Cundari, Y. Surendranath, ACS Catal. 2020, 10, 14782 – 14792; c) R. S. Kim, E. C. Wegener, M. C. Yang, M. E. O'Reilly, S. Oh, C. H. Hendon, J. T. Miller, Y. Surendranath, J. Am. Chem. Soc. 2020, 142, 20631 – 20639; d) M. E. O'Reilly, R. S. Kim, S. Oh, Y. Surendranath, ACS Cent. Sci. 2017, 3, 1174 – 1179.

10. K. J. H. Young, J. Oxgaard, D. H. Ess, S. K. Meier, T. Stewart, I. I. I. W. A. Goddard, R. A. Periana, Chem. Commun. 2009, 3270 – 3272.

11. a) R. A. Periana, D. J. Taube, S. Gamble, H. Taube, T. Satoh, H. Fujii, Science 1998, 280, 560 – 564; b) O. A. Mironov, S. M. Bischof, M. M. Konnick, B. G. Hashiguchi, V. R. Ziatdinov,

W. A. Goddard, M. Ahlquist, R. A. Periana, J. Am. Chem. Soc. 2013, 135, 14644 – 14658; c) R. S. Kim, Y. Surendranath, ACS Cent. Sci. 2019, 5, 1179 – 1186.

12. a) G. B. Shul'pin, A. E. Shilov, G. Süss-Fink, Tetrahedron Lett. 2001, 42, 7253 – 7256; b) C. J. Jones, D. Taube, V. R. Ziatdinov, R. A. Periana, R. J. Nielsen, J. Oxgaard, W. A. Goddard III, Angew. Chem. Int. Ed. 2004, 43, 4626 – 4629; Angew. Chem. 2004, 116, 4726 – 4729.

13. M. N. Vargaftik, I. P. Stolarov, I. I. Moiseev, J. Chem. Soc. Chem. Commun. 1990, 1049 – 1050. [14] a) M. Drees, T. Strassner, J. Org. Chem. 2006, 71, 1755 – 1760; b) M. D. Khokhar, R. S. Shukla, R. V. Jasra, J. Mol. Catal. A 2009, 299, 108 – 116.

15. a) T. Osako, E. J. Watson, A. Dehestani, B. C. Bales, J. M. Mayer, Angew. Chem. Int. Ed. 2006, 45, 7433 – 7436; Angew. Chem. 2006, 118, 7593 – 7596; b) Q. Yuan, W. Deng, Q. Zhang, Y. Wang, Adv. Synth. Catal. 2007, 349, 1199 – 1209.

16. W. M. Haynes, CRC Handbook of Chemistry and Physics, 97th ed., CRC Press/Taylor & Francis, Boca Raton, Florida, 2016.

17. P. Połczyn´ski, R. Jurczakowski, W. Grochala, Chem. Commun. 2013, 49, 7480 – 7482.

18. a) P. Xu, S. Guo, L. Wang, P. Tang, Angew. Chem. Int. Ed. 2014, 53, 5955 – 5958; Angew. Chem. 2014, 126, 6065 – 6068; b) Q.-Z. Zheng, N. Jiao, Chem. Soc. Rev. 2016, 45, 4590 – 4627; c) P. Leszczynski, A. K. Budniak, W. M. Adamczyk, J. H. Gawrackzynski, T. E. Gilewski, P. Polyczynski, R. R. Jurczakowski, W. R. Grochala, Z. Mazej (University of Warsaw), WO 2017/042624 Al, 2017.

19. a) W. Grochala, Phys. Status Solidi B 2006, 243, R81 – R83; b) P. Połczyn´ski, R. Jurczakowski, W. Grochala, J. Phys. Chem. C 2013, 117, 20689 – 20696.

20. a) N. Sauermann, T. H. Meyer, Y. Qiu, L. Ackermann, ACS Catal. 2018, 8, 7086 – 7103; b) C. Ma, P. Fang, T.-S. Mei, ACS Catal. 2018, 8, 7179 – 7189.

21. P. Połczyn´ski, T. E. Gilewski, J. Gawraczyn´ski, M. Derzsi, P. J. Leszczyn´ski, W. Gadomski, Z. Mazej, R. Jurczakowski, W. Grochala, Eur. J. Inorg. Chem. 2016, 5401 – 5404.

22. B. S. Natinsky, S. Lu, E. D. Copeland, J. C. Quintana, C. Liu, ACS Cent. Sci. 2019, 5, 1584 – 1590.

23. E. S. Rountree, B. D. McCarthy, T. T. Eisenhart, J. L. Dempsey, Inorg. Chem. 2014, 53, 9983 – 10002.

24. a) W. Grochala, J. Fluorine Chem. 2008, 129, 82 – 90; b) P. J. Malinowski, M. Derzsi, Z. Mazej, Z. Jaglicˇic´, B. Gaweł, W. Łasocha, W. Grochala, Angew. Chem. Int. Ed. 2010, 49, 1683 – 1686; Angew. Chem. 2010, 122, 1727 – 1730; c) W. Grochala, J. Supercond. Novel Magn. 2018, 31, 737 – 752.

25. N. Elgrishi, K. J. Rountree, B. D. McCarthy, E. S. Rountree, T. T. Eisenhart, J. L. Dempsey, J. Chem. Educ. 2018, 95, 197 – 206.

26. A. Abragam, B. Bleaney, Electron Paramagnetic Resonance of Transition Ions, OUP, Oxford, 2012.

27. A. Sen, M. A. Benvenuto, M. Lin, A. C. Hutson, N. Basickes, J. Am. Chem. Soc. 1994, 116, 998 – 1003.

28. J. B. Allen, R. F. Larry, Electrochemical Methods: Fundamentals and Applications, 2nd ed., Wiley, Hoboken, 2001.

29. S. J. Meek, C. L. Pitman, A. J. M. Miller, J. Chem. Educ. 2016, 93, 275 – 286.

30. a) C. Costentin, S. Drouet, M. Robert, J.-M. Savéant, J. Am. Chem. Soc. 2012, 134, 11235 – 11242; b) J.-M. Savéant, Elements of Molecular and Biomolecular Electrochemistry, Wiley, Hoboken, 2006; c) C. Tsay, J. Y. Yang, J. Am. Chem. Soc. 2016, 138, 14174 – 14177.

31. W. Grochala, Z. Mazej, Philos. Trans. R. Soc. London Ser. A 2015, 373, 20140179.

32. a) J. E. House, K. A. House, Descriptive Inorganic Chemistry, 3rd ed., Academic Press, Boston, 2016, pp. 245 – 268; b) J. Zhu, K. K. Hii, K. Hellgardt, ACS Sustainable Chem. Eng. 2016, 4, 2027 – 2036; c) I. M. Kolthoff, I. K. Miller, J. Am. Chem. Soc. 1951, 73, 3055 – 3059.

33. J. Rostrup-Nielsen, L. J. Christiansen, Concepts in Syngas Manufacture, Imperial College Press, London, 2011.

Supporting information References:

1. a) T. Zimmermann, M. Bilke, M. Soorholtz, F. Schüth, ACS Catal. 2018, 8, 9262-9268; b) B. H. Patel, P. Paricaud, A. Galindo, G. C. Maitland, Ind. Eng. Chem. Res. 2003, 42, 3809- 3823; c) T. D. O'Sullivan, N. O. Smith, J. Phys. Chem. 1970, 74, 1460-1466; d) Z. Duan, N. Møller, J. Greenberg, J. H. Weare, Geochim. Cosmochim. Ac 1992, 56, 1451-1460; e) R. Battino, H. L. Clever, Chem. Rev. 1966, 66, 395-463.

2. A. Sen, M. A. Benvenuto, M. Lin, A. C. Hutson, N. Basickes, J. Am. Chem. Soc. 1994, 116, 998-1003.

3. P. Połczyński, R. Jurczakowski, W. Grochala, J. Phys. Chem. C 2013, 117, 20689-20696.

4. E. Mentasti, C. Baiocchi, J. S. Coe, Coordin. Chem. Rev. 1984, 54, 131-157.

5. A. Abragam, B. Bleaney, Electron Paramagnetic Resonance of Transition Ions, OUP, Oxford, 2012.

6. S. J. Meek, C. L. Pitman, A. J. M. Miller, J. Chem. Edu. 2016, 93, 275-286.

7. P. Zanello, C. Nervi, F. F. de Biani, Inorganic Electrochemistry: Theory, Practice and Application, RSC, Cambridge, UK, 2003.

8. a) C. Costentin, S. Drouet, M. Robert, J.-M. Savéant, J. Am. Chem. Soc. 2012, 134, 11235-11242; b) J.-M. Savéant, Elements of Molecular and Biomolecular Electrochemistry, J. Wiley & Sons, Inc., Hoboken, NJ, 2006; c) C. Tsay, J. Y. Yang, J. Am. Chem. Soc. 2016, 138, 14174-14177.

9. a) M. E. O'Reilly, R. S. Kim, S. Oh, Y. Surendranath, ACS Cent. Sci. 2017, 3, 1174-1179; b) J. B. Allen, R. F. Larry, Electrochemical Methods: Fundamentals and Applications, 2nd ed., John Wiley & Sons, 2001.

10. C. Liang, C. J. Bruell, M. C. Marley, K. L. Sperry, Chemosphere 2004, 55, 1213-1223.

11. L. Dogliotti, E. Hayon, J. Phys. Chem. 1967, 71, 2511-2516.

12. G. E. Walrafen, W. H. Yang, Y. C. Chu, M. S. Hokmabadi, J. Solut. Chem. 2000, 29, 905-936.

13. P. W. Atkins, J. De Paula, J. Keeler, Atkins' Physical Chemistry, 11th ed., OUP, Oxford, 2018.

14. J. P. Guthrie, Can. J. Chem. 1978, 56, 2342-2354.

15. J. Deng, S.-C. Lin, J. Fuller, J. A. Iñiguez, D. Xiang, D. Yang, G. Chan, H. M. Chen, A. N. Alexandrova, C. Liu, Nat. Commun. 2020, 11, 3686. S37

16. R. S. Kim, Y. Surendranath, ACS Cent. Sci. 2019, 5, 1179-1186.

17. R. A. Periana, D. J. Taube, E. R. Evitt, D. G. Löffler, P. R. Wentrcek, G. Voss, T. Masuda, Science 1993, 259, 340.

18. R. A. Periana, O. Mironov, D. Taube, G. Bhalla, C. J. Jones, Science 2003, 301, 814.

19. C. J. Jones, D. Taube, V. R. Ziatdinov, R. A. Periana, R. J. Nielsen, J. Oxgaard, W. A. Goddard III, Angew. Chem. Int. Ed. 2004, 43, 4626-4629; Angew. Chem. 2004, 116, 4726-4729.

20. R. A. Periana, D. J. Taube, S. Gamble, H. Taube, T. Satoh, H. Fujii, Science 1998, 280, 560-564.

21. J. T. Fuller, S. Butler, D. Devarajan, A. Jacobs, B. G. Hashiguchi, M. M. Konnick, W. A. Goddard, J. Gonzales, R. A. Periana, D. H. Ess, ACS Catal. 2016, 6, 4312-4322.

22. S. Chempath, A. T. Bell, J. Am. Chem. Soc. 2006, 128, 4650-4657.

23. O. A. Mironov, S. M. Bischof, M. M. Konnick, B. G. Hashiguchi, V. R. Ziatdinov, W. A. Goddard, M. Ahlquist, R. A. Periana, J. Am. Chem. Soc. 2013, 135, 14644-14658

Conclusion

Both projects are fundamentally the same in that they focus on the generation of liquid MHS from gaseous methane gas. However, as previously stated, each project uses a different transition metal catalyst, the second chapter focused on the use of a vanadium oxo species, and chapter 3 focused on the use of a silver molecular species.

For the case of the vanadium catalysts, the ambient condition of reported catalysis facilitates the use of O_2. Additionally, an added potential benefit is the use of ambient natural gas feedstock for onsite functionalization and independent of a large infrastructure. One aspect that needs to be researched further in the future is scaling up. Additional fundamental and engineering investigations will allow us to explore the possible application of converting CH_4 into commodity chemicals with minimal infrastructure. This can possibly lead to more efficient usage of green-house gases and reducing their emission into atmosphere.

For the silver molecular catalysts, we explored the electrocatalytic CH_4 functionalization mediated by Ag^{II} metalloradical. Through Kinetic characterization we saw that the selective electrocatalytic CH_4 activation in 98% H_2SO_4 and in ambient temperature and room pressure has a low activation energy and high kinetic rate constant. However, additional experiments must be conducted in order to investigate the reactions after the turnover-limiting step after the CH_4 activation. As stated above in chapter 3, there is a mass transport and solubility of CH_4 gas limitation that prevents the maximization of the selectivity in this electrochemical reaction. Furthermore, this work with the silver catalyst can provide a new path towards ambient electrocatalytic CH_4 functionalization and potentially a strategy that can possibly one day applicable for future catalyst design to successfully achieve chemical production from widely distributed natural gas resources with minimal infrastructure.

A future direction that this project can take is to continue studying different transition metal species to see if there another transition metalworks better as a catalyst. Additionally, it would be interesting to possible conduct a study of combining both vanadium and silver in an electrochemical reaction to see if there is a synergistic effect of having both species present.